

OFF-RESONANCE NMR ON ^{15}N IN
GUANOSINE AND PHASE CYCLING OF
QUADRUPOLAR NMR ON ^{17}O IN SILICA

A dissertation

submitted by

Peter Lorenzo Malavé

In partial fulfillment of the requirements
for the degree of

Doctor of Philosophy

in

Physics

TUFTS UNIVERSITY

August 2011

Abstract

OFF-RESONANCE NMR ON ^{15}N IN GUANOSINE and PHASE CYCLING OF QUADRUPOLEAR NMR ON ^{17}O IN SILICA

Nuclear magnetic resonance in the solid state provides a wealth of inter- and intramolecular interactions that can be utilized to provide useful physical information. Chemical shift, dipolar, J-coupling, and quadrupolar interactions are all present in the solid state and provide complementary information on molecular structure and dynamics. In this work, dipolar, J-coupling, and quadrupolar interactions are studied. Lee-Goldburg off-resonance excitation is employed on a sample of ^{15}N enriched guanosine to determine inter and intramolecular nitrogen-hydrogen distances and the scalar J-coupling constant. Satellite transition magic angle spinning is employed on an ^{17}O enriched sample in silica to experimentally study phase cycling effects.

Lee-Goldburg decoupling on guanosine is employed to determine scalar coupling in ^{15}N bonded to ^1H in guanosine. Experimental results are compared to theoretically predicted results. Results show scaling factors of 0.47 ± 0.03 and 0.39 ± 0.13 compared to theoretical values of 0.58. Also, a hydrogen bond shift in the resonance frequencies is postulated.

Lee-Goldburg cross polarization on guanosine is used to probe inter-nuclear distances of ^{15}N bonded to ^1H in guanosine. Results are compared to x-ray

crystal structures where positions of protons are energetically optimized. Simulation of experimental results is also used to compare x-ray bond lengths to Lee-Goldburg cross polarization results. The Lee-Goldburg results for N-H and N-H₂ bonds show stronger agreement with simulation than x-ray results. Differences in distances range from 0.01 to 0.05 Å. N-H hydrogen bond distances are also compared.

Finally, phase cycling effects are studied in satellite transition magic angle spinning experiments on ¹⁷O in silica. Results show that a variety of phase cycles for the final pulse in the pulse sequence can be employed to give quantitatively the same result. On the other hand, phase cycles for the first and second pulses may significantly alter the spectrum, showing more coherences for smaller numbers of phase cycles.

Acknowledgments

Firstly and most importantly, I need to acknowledge and thank my parents, Mary Lou and Santos Malavé. Your constant support, unconditional love, and encouragement throughout my life has given me not only strength, but the most perfect example of how to live and love. Vos amo mas que cualquier cosa en este mundo. Thanks also to my brothers and sisters, Santos, Maureen, Siobhan, and Danny who in no small way helped to fashion the person I am today. To David Grant, one of my two advisors, who probably saved me from leaving the PhD program at Tufts. To my advisor at Tufts, William Oliver, who supported me in my long distance research. To Bernie Gerstein for many helpful discussions over music and wine. To the Burlingame Foundation, for a year of financial support early on in my studies. To the late David Weaver who initially took me under his wing. To NIH General Medical Sciences under award of RO1 08521 which funded the work of the Grant lab.

Contents

1	Introduction	12
2	Solid State Nuclear Magnetic Resonance	18
2.1	Elementary Nuclear Magnetic Resonance Theory	19
2.2	Tensors and Notation	22
2.3	Experimental Nuclear Magnetic Resonance	27
2.3.1	Hardware and Acquisition	27
2.3.2	RF Pulses and Pulse Sequences	28
2.3.3	Analysis	30
2.3.4	Sample Spinning	32
2.4	Spin Interactions	34
2.4.1	Chemical Shielding	34
2.4.2	J-Coupling	38
2.4.3	Dipolar Coupling	39
2.4.4	Quadrupolar Hamiltonian	40
2.5	The Density Matrix	41
2.5.1	Creation of Quantum Coherence	44
2.5.2	Detection of Quantum Coherence	48
3	The Quantum Coherence Experiment	52
3.1	Perturbation Terms in The Quadrupolar Hamiltonian	53

3.2	Satellite Transitions	54
3.2.1	Satellite Transition Experiment	55
3.3	Results of Silica Phase Cycling STMAS	56
4	The Lee-Goldburg Experiment	64
4.1	Decoupling	64
4.1.1	General Decoupling	65
4.1.2	Lee-Goldburg Decoupling	65
4.2	J-Coupling Results in Guanosine	67
4.3	Lee-Goldburg Cross Polarization	77
4.3.1	Cross Polarization	77
4.3.2	Lee-Goldburg Cross Polarization	79
4.4	Results Dipolar Coupling in Guanosine	79
5	Conclusions	86

List of Figures

2.1	Graphical representation of a pulse sequence. Vertical axis represents relative strength of the pulse in arbitrary units. Horizontal axis represents time in arbitrary units.	29
2.2	The free induction decay of ^{13}C in adamantane. Data taken on a Varian 400 Mhz spectrometer.	31
2.3	The spectrum of ^{13}C in adamantane. Two peaks are present due to there being two ^{13}C nuclei with differing resonance frequencies.	31
2.4	Spinning sidebands in the spectrum of ^{15}N in glycine.	33
2.5	Spinning sidebands in the spectrum of ^{15}N in glycine.	34
2.6	Static powder pattern of ^{13}C in glycine. Data was taken on a 9.4 T magnet. The vertical axis is the magnitude squared of the Fourier transform of the time domain signal. Note the breadth of the spectrum ≈ 14 kHz.	37
2.7	Spectrum of ^{13}C in glycine with the powder pattern removed by sample spinning and decoupling. Data was taken on a 9.4 T magnet. The vertical axis is the magnitude squared of the Fourier transform of the time domain signal. Note the breadth of the spectrum ≈ 100 Hz.	37
2.8	Graphical depiction of the coherence transfer pathway for a single pulse.	51

3.1	Energy level diagram for a spin $\frac{5}{2}$ nucleus. CT is the central transition. ST_n in the n^{th} satellite transition.	54
3.2	The 1QSTMAS pulse sequence and coherence transfer pathway. The ϕ_i are the pulse phases about the z-axis. The t_1 variable is incremented to give a 2-dimensional spectrum.	55
3.3	Schematic of possible results from a 1QSTMAS experiment performed on a spin $\frac{5}{2}$ nucleus. F_1 and F_2 are the Fourier transformed t_1 and t_2 dimensions. The slope of lines in the spectrum are calculated as the ratio, R , of second order rank 4 broadenings of the transitions involved. Thus $R = 1$ for CT-CT, $R = 7/24$ for ST_1 -CT, and $R = -11/6$ for ST_2 -CT.	57
3.4	Shearing of STMAS spectrum. The spectrum has been rotated so that the $ST-1$ -CT portion gives the isotropic projection on the F_1 axis.	58
3.5	The 1QSTMAS spectra of ^{17}O in 10% enriched SiO_2 . Experiments were performed on a 14.09 T magnet.	59
3.6	The projection of Figure 3.5 along the F_2 axis.	59
3.7	The projection of Figure 3.5 along the F_1 axis.	60
3.8	The spectrum for one value of ϕ_2 . The boxed area shows a CT-CT line not apparent in the 4 phase cycle spectrum. . . .	61
3.9	The spectrum for two values of ϕ_2 . The CT-CT coherence line is still apparent.	62
3.10	The spectrum for one value of ϕ_1	62
3.11	The spectrum for two values of ϕ_1	63
4.1	Representation of Lee-Goldburg vectors in the rotating frame.	66
4.2	Guanosine molecule with the N1-H1 portion highlighted and the ^{15}N spectrum with resonance peaks labeled.	69

4.3	Molecules of guanosine showing orientation in the crystal for the N1-N7 hydrogen bond. Highlights show the nitrogen and hydrogen atoms involved in the hydrogen bond.	70
4.4	Guanosine ^{15}N cross polarization with LG decoupling.	72
4.5	Guanosine N1 peaks for TPPM and LG decoupled data. The TPPM decoupled data was magnified 10 times to make comparison more clear.	72
4.6	Fitting of the N-H splitting in the Lee-Goldburg decoupled spectrum of guanosine.	73
4.7	The fitted guanosine spectrum of TPPM decoupled data.	75
4.8	The fitted guanosine spectrum of LG decoupled data.	75
4.9	The cross polarization pulse sequence. A $\frac{\pi}{2}$ pulse is applied to the abundant I spins before the cross polarization pulses are applied.	78
4.10	The Lee-Goldburg cross-polarization spectra of ^{15}N in 100% enriched guanosine.	80
4.11	The Lee-Goldburg cross-polarization cross section for an N1 peak in guanosine.	81
4.12	SPINEVOLUTION simulation for an N-H dipolar coupled bond with bond length of 1.04 \AA	81
4.13	SPINEVOLUTION simulation for an N-H dipolar coupled bond with bond lengths from 1.02 to 1.06 \AA	82
4.14	The Lee-Goldburg cross-polarization cross section for an N2 peak in guanosine.	83
4.15	SPINEVOLUTION simulation for an N-H ₂ dipolar coupled bond with bond lengths of 1.07 and 1.07 \AA	83

4.16	SPINEVOLUTION simulation for an N-H ₂ dipolar coupled bonds. One bond was held fixed at $\overset{\circ}{\text{A}}$ while the other was varied with bond lengths from 1.05 to 1.09 $\overset{\circ}{\text{A}}$	84
4.17	SPINEVOLUTION simulation for an N-H ₂ dipolar coupled bonds with bond lengths of 1.01 and 1.02 $\overset{\circ}{\text{A}}$	84
4.18	The Lee-Goldburg cross polarization cross section for N7.	85
4.19	SPINEVOLUTION simulation for hydrogen bond lengths. Length units are in $\overset{\circ}{\text{A}}$	85

Chapter 1

Introduction

Nuclear magnetic resonance (NMR) enjoys a wide variety of applications in physics, chemistry, biology, and medicine. The first experimental results in 1936 by Rabi opened the doors to greater understanding of the interplay between quantum spin and magnetic fields in matter. It was thought early on that once the resonance of a nucleus was determined, there were no other important applications of NMR. In fact, it was a great surprise to the early investigators that a nucleus would exhibit measurably different magnetic resonances depending on the molecular environment [30]. Since then NMR has enjoyed rebirths many times over and continues to be a very active area of research and application.

Continuing interest in NMR is due to the great wealth of nuclear interactions which lend themselves to measurement. In the solid state, Zeeman, chemical shift, dipolar, J-coupling, and quadrupolar interactions are all present and observable. Each provides important structural and dynamic information for electrons, nuclei, and molecules. The Zeeman interaction which describes the interaction between the spin of the bare nucleus and an external magnetic field provides a means of measuring the nuclear magneton. Chemical shift is the

interaction resulting from the electronic clouds reacting to the magnetic field. It was the chemical shift which gave early investigators the surprising array of nuclear resonances for various chemical environments. Dipolar interactions involve spin couplings between nuclei and their mutual magnetic fields. This interaction is useful for determining internuclear distances. The J-coupling interaction involves spin interactions between nuclei through the electron spins in their shared bonds. Lastly, a nucleus with a quadrupole moment interacts with the field gradient of its electronic cloud giving a quadrupolar interaction.

Coupling of nuclear magnetic dipoles have traditionally been considered a bane to high resolution NMR spectroscopists. These interactions are responsible for broadening of the spectrum and much work has gone into removing, or decoupling dipolar interactions from the spectrum [25]. Removal of dipolar coupling is accomplished either physically or by application of pulsed radio frequency magnetic fields. Physically, spinning a sample via an air motor about an axis inclined to the applied static magnetic field effectively removes dipolar couplings. Radio frequency methods typically remove dipolar coupling with a combination of on-resonance pulses, changes in pulse phases, and sample spinning [3, 5]. However, reduction or removal of certain dipolar couplings can also be accomplished with off-resonance excitation and sample spinning. Lee and Goldburg first used off-resonance excitation to remove homonuclear dipole coupling [26]. Lee-Goldburg cross polarization and decoupling has since been applied to solids.

Waugh developed the separated local field experiment and was the first to utilize Lee-Goldburg cross polarization and dipolar coupling to determine distances between nuclei [22]. This was seen as an interesting use of dipolar coupling, but not thought of as very useful, since x-ray crystallography was the tool of choice for structure determination [4]. As instrumentation and

technique has improved, NMR measurement of molecular structure has likewise improved. X-ray crystallography gives very good information on nuclear positions for atoms heavier than hydrogen. However, it is not capable of providing position information for hydrogen nuclei. It also has a drawback in that samples must form good crystals. Solid state NMR on the other hand can provide positions of potentially all nuclei and samples need not necessarily be crystalline [43].

Interest in biomolecular structures has blossomed over the past few decades. The structure-function relationship in biomolecules is of great interest [2]. Many times, biomolecular samples are either amorphous or microcrystalline and do not lend themselves to x-ray crystallography [2]. Liquid state NMR has been a boon in this area. Likewise, Solid state NMR is seeing a resurgence of interest in determining structure providing detail on larger distances than liquid NMR, since the inherent motion in liquids obscures intermolecular distances. In solids, studies have been focused on C-H bonding structures with relatively little work on N-H systems and hydrogen bonded structures. In this work, N-H bonded systems in ^{15}N labeled guanosine are studied to give distance measurements.

Guanosine, being a nucleoside, is well studied and does lend itself to x-ray crystallography. Guanosine also includes a variety of N-H bonds as well as hydrogen bonds. This makes it an ideal system to compare x-ray and NMR data while at the same time furthering the applicability of NMR crystallography. Although guanosine has been well studied, its ability to hydrogen bond to other guanosine molecules and other nucleosides has recently been taken advantage of in the area of organic semiconductors and nanotechnology [17, 42]. This capability to hydrogen bond may make it useful for biomolecular detection in semiconductor electronic devices [17]. As electronic interactions

are important in the breaking and forming of hydrogen bonds, the J-coupling interaction is a source of important local bond information [11, 41]. The J-coupling interaction is routinely measured in liquids. However in solids, it is small in comparison to the other interactions and therefore relatively hard to measure. In this work, a scalar coupling in the N-H of guanosine has been measured with Lee-Goldburg decoupling.

Guanosine is currently used in organically modified silicon-based semiconductors [39]. A solution of guanosine is placed between electrodes on a silica, SiO₂, substrate. As it evaporates, a guanosine crystal is formed on the silica, spanning the electrodes. Both the guanosine crystal and the silica substrate are amenable to study by solid state NMR. The ¹⁷O isotope of oxygen is quadrupolar with a spin of $\frac{5}{2}$. The quadrupolar interaction is very sensitive to local electronic changes [34]. Thus, it could provide useful information on silica in conjunction with guanosine in the area of organic semiconductors. With an eye towards understanding spin interactions in a guanosine-silica semiconductor, a sample of ¹⁷O enriched silica makes an ideal system for study.

Quadrupolar interactions can be as large as or larger than chemical shift and dipolar interactions. Thus, quadrupolar nuclei typically exhibit broad spectra which lack resolution. To resolve quadrupolar spectra, there exist a number of methods, most notably multiple quantum NMR experiments. Multiple quantum experiments are so named because they take advantage of the multiple spin states that characterize quadrupolar nuclei and the coherences that can be created between spin states. The first multiple quantum experiment was performed in 1995 [24]. This experiment was called multiple quantum magic angle spinning and utilized symmetric spin state transitions. A more recent multiple quantum experiment taking advantage of asymmetric spin state transitions, termed the satellite transition magic angle spinning

experiment was introduced in 2000 [55].

Satellite transition magic angle spinning experiments have an advantage over multiple quantum magic angle spinning of generally having greater efficiency [45]. Though satellite transition experiments have been applied to a variety of spin systems with very good increase in resolution, there have not been any studies in phase cycling effects on the spectrum in these experiments. In this work, I look at the effects of phase cycling in a satellite transition experiment on a ^{17}O enriched sample of silica.

The field of NMR has a breadth and depth that is astounding. It is vibrant and growing. This thesis will cover the theoretical basics of solid state NMR including the nuclear interactions and some mathematical notation which enables a salient discussion. A discussion of general experimental considerations including apparatus, signal analysis, and sample spinning is included to give background on typical NMR experiments. The important theoretical concepts involved in multiple quantum coherence are developed to give background for satellite transition experiments. The satellite transition multiple quantum experiment is then discussed and results of experiments are presented. Next, the experimental implementations of Lee-Goldburg decoupling and cross polarization are discussed. Penultimately, the results of Lee-Goldburg experiments on guanosine are presented. The Lee-Goldburg decoupling experiment measures the J-coupling constant for N-H bonds, and Lee-Goldburg cross polarization measures bond distances, including hydrogen bonds.

Figures of spectra in this work were created with MATLAB. Analysis was also carried out with MATLAB.

Acronyms Used in This Work

B3LYP	3 parameter Becke-Lee-Yang-Parr
CP	Cross Polarization
CT	Central Transition
DFT	Density Functional Theory
EFG	Electric Field Gradient
ESD	Energy Spectral Density
FWHM	Full Width at Half Maximum
LG	Lee-Goldburg
LGCP	Lee-Goldburg Cross Polarization
MQMAS	Multiple Quantum Magic Angle Spinning
NMR	Nuclear Magnetic Resonance
PAS	Principal Axis System
SSNMR	Solid State Nuclear Magnetic Resonance
ST	Satellite Transition
STMAS	Satellite Transition Magic Angle Spinning
TPPM	Two Pulse Phase Modulation
1QSTMAS	Single Quantum Satellite Transition Magic Angle Spinning

Chapter 2

Solid State Nuclear Magnetic Resonance

Nuclear magnetic resonance (NMR) is a direct consequence of the Zeeman Effect. It finds application in all phases of matter. This work deals solely with solid state nuclear magnetic resonance (SSNMR). Unlike liquid and gas phase NMR, SSNMR reveals the effects of magnetic dipolar, electronic, and quadrupolar interactions. These interactions add more complexity to a spectrum. SSNMR arguably gives the richest and most complicated of resonance spectra.

NMR on solids is done on both single and powdered crystals. Powdered samples give rise to what are called powder patterns in the spectrum. These are broad spectra that encode information from the electronic shielding, dipolar, and quadrupolar interactions of the nuclei and electrons. Single crystal samples show a particular frequency from the powder pattern based on the orientation of the crystal to the Zeeman field.

This chapter covers the essential elements of SSNMR. It starts with an elementary description of NMR theory. Next, it describes interactions which

provide complexity in solid state spectra: electronic, dipolar, and quadrupolar interactions. Finally, it relays basic experimental considerations.

2.1 Elementary Nuclear Magnetic Resonance Theory

A quantum mechanical particle with a non-zero spin subjected to a constant magnetic field will exhibit the Zeeman effect. The Zeeman Hamiltonian is given by

$$\mathcal{H}_z = -\boldsymbol{\mu} \cdot \mathbf{B} \tag{2.1}$$

where $\boldsymbol{\mu} = \gamma \mathbf{I}$ is the quantum mechanical spin magnetic moment with γ the gyromagnetic ratio and \mathbf{I} the intrinsic spin angular momentum. \mathbf{B} is the magnetic field. As a model system, take a spin $\frac{1}{2}$ particle with $\gamma < 0$ and the magnetic field $\mathbf{B} = (0, 0, B_z)$ constant in time and space. This system exhibits two energy levels in the presence of a magnetic field. The difference between the energy levels is $\Delta E = \hbar\omega = -\gamma B_z \Delta I_z$, and as exhibited in Equation 2.1, only depends on the component of spin along \mathbf{B} . In a constant magnetic field an ensemble of quantum mechanical particles with non-zero spin will be found distributed between two energy levels. At equilibrium, the distribution will be Boltzmann.

We are now concerned with how to generate a state transition. For transitions to take place, energy must be added to and/or taken away from the system. Therefore we consider a time dependent Hamiltonian,

$$\mathcal{H}_z(t) = -\boldsymbol{\mu} \cdot \mathbf{B}(t) \tag{2.2}$$

Letting $\mathbf{B}(t) = B_{rf} \cos(\omega_{rf}t)\hat{i} + B_{rf} \sin(\omega_{rf}t)\hat{j} + B_0\hat{z}$, we have a rotating radio frequency (rf) magnetic field in the xy plane and a constant field in the z direction. Applying this to the Schroedinger equation,

$$i\hbar \frac{\partial \Psi}{\partial t} = \hat{H}_z(t)\Psi \quad (2.3)$$

$$= -\gamma\hbar[B_0I_z + B_{rf}(I_x \cos(\omega_{rf}t) + I_y \sin(\omega_{rf}t))]\Psi \quad (2.4)$$

$$= -\gamma\hbar[B_0I_z + B_{rf}e^{-i\omega_{rf}I_z t}I_x e^{i\omega_{rf}I_z t}]\Psi \quad (2.5)$$

The final equation follows from the relation [31]

$$[A, B] = i\xi C \quad (2.6)$$

$$e^{-i\theta A} B e^{i\theta A} = B \cos \xi\theta + C \sin \xi\theta \quad (2.7)$$

Equation 2.5 is in a mixed Schroedinger/Heisenberg representation. We can transform it to a Schroedinger representation using

$$\Psi' = e^{i\omega_{rf}I_z t}\Psi \quad (2.8)$$

$$\Psi = e^{-i\omega_{rf}I_z t}\Psi' \quad (2.9)$$

This gives

$$\frac{\partial \Psi}{\partial t} = -i\omega_{rf}I_z e^{-i\omega_{rf}I_z t}\Psi' + e^{-i\omega_{rf}I_z t}\frac{\partial \Psi'}{\partial t} \quad (2.10)$$

Using this and multiplying from the left with $e^{i\omega_{rf}I_z t}$, the Schroedinger equation becomes

$$i\hbar \frac{\partial \Psi'}{\partial t} = -[\hbar(\omega_{rf} + \gamma B_0)I_z + \gamma\hbar B_{rf}I_x]\Psi' \quad (2.11)$$

This form of the equation serves to point out two features of the system. The operator I_x rewritten in the form of raising and lowering operators, $I_x = \frac{I^+ + I^-}{2}$, shows that we get state transitions for non-zero B_{rf} . Second, it is cast in a

form where the original wave function has been transformed by a rotation operator, $e^{i\omega_{rf}I_z t}$. This operator rotates the wave function about the z axis, or in other words, the spin angular momentum of the particle corresponds to a non-zero $\langle I_z \rangle$. We call the reference system of Ψ' the rotating reference frame. It rotates with the frequency ω_{rf} . The Zeeman Hamiltonian in the rotating frame is $\hat{H}_z^{rot} = -[\hbar(\omega_{rf} + \gamma B_0)I_z + \gamma\hbar B_{rf}I_x]$. It takes a particularly simple form if we let $\omega_{rf} = -\gamma B_0$,

$$\hat{H}_z^{rot} = -\gamma\hbar B_{rf}I_x \quad (2.12)$$

In this case, the applied rf field is said to be on resonance. This terminology comes from the fact that the resonance condition is achieved when the energy of the applied rf field exactly matches the difference in energy levels of a two level system. Using the relation in Equation 2.7, the effect of such a Hamiltonian on the operator I_z is

$$e^{-i\omega I_x} I_z e^{i\omega I_x} = -I_y \sin \omega t + I_z \cos \omega t \quad (2.13)$$

where $\omega = -\gamma B_{rf}$. This shows that spin operator components will mix with an applied transverse magnetic field, giving rise to non-zero spin states in the transverse direction. For an ensemble of spins, a magnetization initially in the z -direction will be transformed to a magnetization in the y -direction. Looked at another way, in the rotating frame a transverse field applied along the x -direction will lead to precession of the spin about the x -axis.

An applied field takes the system out of its equilibrium distribution. If this field is then removed, the spin system will again return to equilibrium over time. Two relaxation mechanisms are responsible for this: spin-lattice and spin-spin relaxation [10]. Spin-lattice relaxation is also known as longitudinal

or T_1 relaxation. It is characterized by the time constant, T_1 , which defines how long it takes for the system to reach equilibrium with the static field. These relaxation processes deal with the exchange of energy between the spins and the lattice environment in which they are situated. Such processes include vibrational and, in metals, conduction electron couplings.

Spin-spin relaxation is also known as transverse or T_2 relaxation. T_2 is the characteristic time for the transverse magnetization to decay to zero. This process is influenced by couplings between the spins themselves. The observation time of an NMR signal is modulated by T_2 . Typically, $T_1 > T_2$, showing that lattice couplings are smaller than spin couplings. The major spin interactions of importance to both relaxation and resonance in NMR are described in Section 2.4.

2.2 Tensors and Notation

This section provides background on tensors and tensor notation that will be used in varying degrees in Sections 2.3.4, 2.4, 2.5, and 3.1. It will provide a mathematical basis for describing the interactions that give rise to the experimental observables in NMR.

In terms of Cartesian tensors, a Hamiltonian for a particular interaction may be represented as [51]

$$\mathcal{H} = C \sum_{\alpha, \beta=1}^3 R_{\alpha\beta} T_{\alpha\beta} \tag{2.14}$$

$$\tag{2.15}$$

\mathbf{T} is a tensor operator which depends on the spin components of the interaction. \mathbf{R} is a tensor operator depending on the geometry of the interaction and

as such characterizes the spatial part of the Hamiltonian. It is therefore a rank 2 tensor and can be decomposed into irreducible components with respect to the rotation group $\text{SO}(3)$,

$$\mathbf{R} = \mathbf{R}^{(0)} + \mathbf{R}^{(1)} + \mathbf{R}^{(2)} \quad (2.16)$$

The terms on the RHS are the zeroth rank, first rank antisymmetric, and second rank symmetric components, respectively. Taking the principal axis system (PAS) to be the one in which $\mathbf{R}^{(2)}$ is diagonal, letting $\boldsymbol{\rho}$ be the PAS representation of \mathbf{R} , and using the traceless property of symmetric matrices, we define

$$R = \frac{1}{3} \text{Tr} \mathbf{R} \quad (2.17)$$

$$\delta = \rho_{zz}^{(2)} \quad (2.18)$$

$$\eta = \frac{\rho_{yy}^{(2)} - \rho_{xx}^{(2)}}{\delta} \quad (2.19)$$

R is the isotropic value, δ is termed the principal value, and η the asymmetry parameter. In the context of NMR, R is the average value of an interaction, δ is the largest component in the interaction, and η describes the asymmetry of an interaction. These parameters will be used to describe spin interactions in Section 2.4.

Spherical tensor operators are useful for transformations between coordinate axes. An irreducible tensor of rank l , T_{lm} , is defined by its properties under rotations, R ,

$$RT_{lm}R^{-1} = \sum_{m'=-l}^l T_{lm'} \mathcal{D}_{m'm}^{(l)} \quad (2.20)$$

where $\mathcal{D}_{m'm}^{(l)}$ is Wigner rotation matrix which depends on Euler angles and the rank of the tensor. A tensor not transforming in this way is not irreducible.

The Hamiltonian expressed in irreducible spherical tensor operators is [19]

$$\mathcal{H} = C \sum_l \sum_{m=-l}^l (-1)^m R_{l-m} T_{lm} \quad (2.21)$$

In the PAS, irreducible spherical components of $\boldsymbol{\rho}$ formulated in terms of the isotropic value, principal value, asymmetry parameters, and other Cartesian components are [19]

$$\rho_{00} = R \quad (2.22)$$

$$\rho_{10} = -i\sqrt{2}\rho_{xy} \quad (2.23)$$

$$\rho_{1\pm 1} = \rho_{xz} \pm i\rho_{yz} \quad (2.24)$$

$$\rho_{20} = \sqrt{\frac{2}{3}}\delta \quad (2.25)$$

$$\rho_{2\pm 1} = 0 \quad (2.26)$$

$$\rho_{2\pm 2} = -\frac{\delta\eta}{2} \quad (2.27)$$

$\rho_{2\pm 1} = 0$ because $\rho^{(2)}$ is completely symmetric. The irreducible operators are expressed in the lab frame using Wigner rotation matrices, $\mathcal{D}(\alpha, \beta, \gamma)$,

$$R_{lm} = \sum_{m'} \mathcal{D}_{m'm}^l(\alpha, \beta, \gamma) \rho_{lm'} \quad (2.28)$$

The arguments of the Wigner matrix being the Euler angles that define the orientation of the PAS to the lab frame. Components of the Wigner matrices are determined as [15]

$$\mathcal{D}_{m'm}^l(\alpha, \beta, \gamma) = e^{-i(\alpha m' + \gamma m)} d_{m'm}^l(\beta) \quad (2.29)$$

d is the reduced Wigner rotation matrix. Its elements are

$$d_{m'm}^l(\beta) = (-1)^{m'-m} \sum_{\mu} (-1)^{\mu} \frac{\sqrt{(l+m)!(l-m)!(l+m')!(l-m')!}}{\mu!(l+m-\mu)!(l-\mu-m')!(m'+\mu-m)!} \cos\left(\frac{\beta}{2}\right)^{2l+m-m'-2\mu} \sin\left(\frac{\beta}{2}\right)^{2\mu+m'-m} \quad (2.30)$$

The summation goes over values of μ such that all the factors in the denominator are of nonnegative integers.

The T_{lm} in the Hamiltonians of interest in this work are formed from the components of first rank irreducible spherical tensors, or in other words, vectors. Their components are determined from Cartesian vector components, V_x, V_y, V_z by

$$V_{10} = V_z \quad (2.31)$$

$$V_{1\pm 1} = \mp \frac{1}{\sqrt{2}}(V_x \pm iV_y) \quad (2.32)$$

For spin operators, these amount to I_z and I^{\pm} . Using the formula for direct products of tensors [28],

$$T_{LM} = \sum_m \langle l_1 m l_2 M - m | l_1 l_2 LM \rangle T_{l_1 m} T_{l_2 M - m} \quad (2.33)$$

where the bra-ket terms are Clebsch-Gordon coefficients, we get the T_{lm} in

terms of first rank tensors \mathbf{V} and \mathbf{U} [19]

$$T_{00} = \frac{1}{\sqrt{3}}(V_{1+1}U_{1-1} + V_{1-1}U_{1+1} - V_{10}U_{10}) \quad (2.34)$$

$$T_{10} = \frac{1}{\sqrt{2}}(V_{1+1}U_{1-1} - V_{1-1}U_{1+1}) \quad (2.35)$$

$$T_{1\pm 1} = \frac{1}{\sqrt{2}}(\pm V_{1\pm 1}U_{10} \mp V_{10}U_{1\pm 1}) \quad (2.36)$$

$$T_{20} = \frac{1}{\sqrt{6}}(V_{1+1}U_{1-1} + V_{1-1}U_{1+1} + 2V_{10}U_{10}) \quad (2.37)$$

$$T_{2\pm 1} = \frac{1}{\sqrt{2}}(V_{1\pm 1}U_{10} + V_{10}U_{1\pm 1}) \quad (2.38)$$

$$T_{2\pm 2} = V_{1\pm 1}U_{1\pm 1} \quad (2.39)$$

Generally for T_{00} , the coefficient is absorbed into the LHS of the equation giving $T_{00} = \mathbf{V} \cdot \mathbf{U}$. For Hamiltonians of interest in NMR, \mathbf{V} and \mathbf{U} are either both spin operators or combinations of a spin operator and a magnetic field vector.

As a simple example of expressing a Hamiltonian in terms of irreducible spherical tensor operators, consider the Zeeman interaction given in Equation 2.1. This equation is simply an inner product of first rank tensors I and B ,

$$\mathcal{H}_z = C_z \sum_l \sum_{m=-l}^l (-1)^m R_{l-m} T_{lm} \quad (2.40)$$

$$= C_z R_{00} T_{00} \quad (2.41)$$

$$= C_z R_{00} (I_{1+1} B_{1-1} + I_{1-1} B_{1+1} - I_{10} B_{10}) \quad (2.42)$$

$$= -C_z R_{00} I_{10} B_{10} \quad (2.43)$$

The second equation comes from the scalar product $I \cdot B = T_{lm}$. The last equation follows from taking $\mathbf{B} = (0, 0, B_z)$ which gives $B_{1\pm 1} = 0$. By comparison with Equation 2.1, $R_{00} = \mathbf{1}$ and $C_z = \gamma$.

2.3 Experimental Nuclear Magnetic Resonance

To observe the interactions of the last section, we require the application of radio frequency (rf) fields to a sample. The hardware produces the fields, allows acquisition, and conditions signals prior to processing. In this chapter, I will describe generic NMR hardware and processing of the data obtained.

2.3.1 Hardware and Acquisition

In order to observe spins, they must be exposed to magnetic fields. The fields important in NMR are the static field and applied field. Static fields are typically generated by an energized superconducting coil. This field defines the z-direction in the lab frame.

Inserted into the most homogeneous area of the static field is the probe. The probe houses another coil which when energized subjects the spins to the applied rf magnetic field. Also within the probe are the electronic components used to adjust the impedance of the rf coil, as well as pneumatic lines and the stator for sample spinning, and optical lines to allow measurement of spinning speed.

To energize the rf coil, a program loaded on a microprocessor dictates the sequence of rf pulses, their timing, frequencies, phases, and power levels. Synthesizers generate the fundamental resonance frequencies. The output of the synthesizers pass through phase shifters that are controlled by the pulse program microprocessor. Pulses of the rf signal are created by gating circuitry controlled by the pulse program. The pulses pass through amplifiers to the rf coil circuit in the probe. This is the flow of the excitation signal to the probe.

During acquisition, the receiver circuits are energized. Precession of the spins within the coil induces a current within the coil via Faraday's Law. This

signal passes from the probe to an amplifier and a receiver. In the receiver, the signal gets down-converted in frequency relative to a reference frequency generated by a crystal oscillator and split into a real and complementary (imaginary) signal. This quadrature (complex) signal makes it possible to distinguish between the frequency of the reference signal provided by the synthesizer and a Larmor frequency greater than or less than the reference frequency. Essentially, it gives the signal a measurable phase that relates to the phase of the synthesizer reference. The signal is then digitized and passes through a phase shifter controlled by the pulse program. Finally the signal passes to a computer for analysis.

2.3.2 RF Pulses and Pulse Sequences

The typical NMR experiment involves setting the timing, frequency, and phase of the rf pulses. The power, duration, and phase of a pulse determines the direction of magnetization of the sample. The frequency is usually chosen to maximize the resonance signal.

In describing the NMR experiment, pulse sequence diagrams are very useful. They can provide enough information to give a general idea of the pulse program, the overall experiment, and hint at the expected outcome. A simple one pulse diagram is provided in Figure 2.1. In this pulse sequence, the diagram depicts an rf pulse width (pw) as well as the phase of the pulse (rf phase) relative to the reference frequency defined for the pulse. Pulse widths and their phases determine the direction of magnetization after their application. We can consider spin operator transformations to describe this mathematically. Pulses produce rotations of $\langle I_z \rangle$ about the direction of B_{rf} , so can be

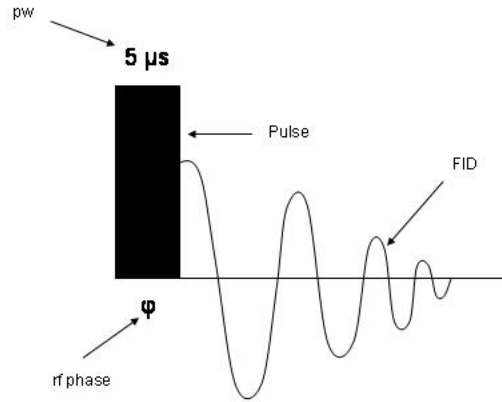


Figure 2.1: Graphical representation of a pulse sequence. Vertical axis represents relative strength of the pulse in arbitrary units. Horizontal axis represents time in arbitrary units.

written as a rotation operator on spins. In general,

$$R(\theta) = e^{-i\theta\hat{\mathbf{n}}\cdot\mathbf{I}} \quad (2.44)$$

This is a rotation by an angle θ about an arbitrary axis defined by $\hat{\mathbf{n}}$. In particular, a rotation of θ about the y-axis is written

$$R(\theta) = e^{-i\theta\hat{\mathbf{y}}\cdot\mathbf{I}} \quad (2.45)$$

$$= e^{-i\theta I_y} \quad (2.46)$$

Experimentally, the rotation angle is determined by the rf pulse power and its duration, i.e. $\theta = \omega t$. The axis of rotation in the rotating frame is determined by the phase of the rf pulse. Using the relation in Equation 2.7, we can

determine the effect of a pulse with $\theta = \frac{\pi}{2}$ and about the y-axis on a spin in the z-direction,

$$e^{-i\theta I_y} I_z e^{i\theta I_y} = I_z \cos \theta + I_x \sin \theta \quad (2.47)$$

$$= I_z \cos \frac{\pi}{2} + I_x \sin \frac{\pi}{2} \quad (2.48)$$

$$= I_x \quad (2.49)$$

Thus, the spin or for an ensemble of spins, the magnetization will be along the x-axis.

2.3.3 Analysis

The NMR signal has the general form

$$s(t) \propto e^{i\omega t} e^{-t/\tau} \quad (2.50)$$

where τ is the time constant of relating to T_2 relaxation. Since $s(t)$ involves a “free” precession of the spins which induce a signal in the rf coil, the signal referred to as a free induction decay (FID). The FID is transformed to the frequency domain using the Fourier transform

$$S(\omega) = \int s(t) e^{-i\omega t} dt \quad (2.51)$$

More precisely, since the FID is a digital signal, the transformation is performed with the discrete Fourier transform. The spectral width of the data are set in the pulse program. Typically, spectra are displayed as $|S(\omega)|^2$ giving the energy spectral density (ESD) as a function of frequency. Spectra displayed as $|S(\omega)|$ gives intensity in arbitrary units as a function of frequency. Both types of representation are used in this work. Also, the x-axis is given in units

of frequency relative to a chosen reference frequency, usually either the pulse frequency or the resonance frequency of a chosen standard. In other words, the x-axis is a frequency shift.

Figure 2.2 and 2.3 show a representative FID and its Fourier transform.

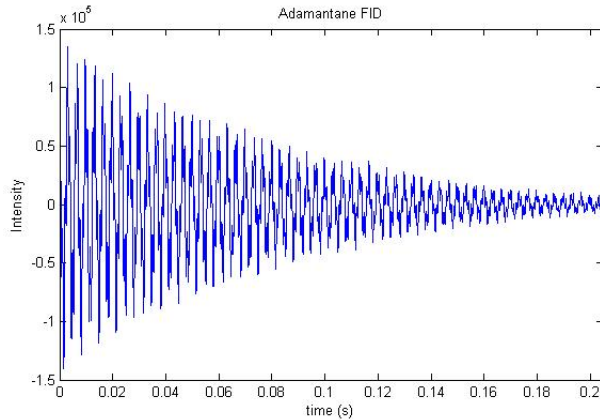


Figure 2.2: The free induction decay of ^{13}C in adamantane. Data taken on a Varian 400 Mhz spectrometer.

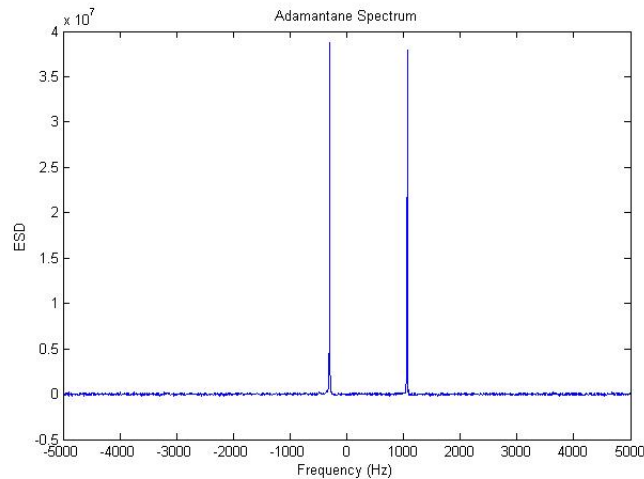


Figure 2.3: The spectrum of ^{13}C in adamantane. Two peaks are present due to there being two ^{13}C nuclei with differing resonance frequencies.

The full width at half max of the spectral lines is indicative of the time constant of the signal and is inversely proportional to the T_2 relaxation time. This is a direct result of Fourier transforming an exponential signal. Exponentials

in the time domain transform to Lorentzians in the frequency domain with a full width at half max inversely proportional to the exponential time constant. Experimentally, a long T_2 relative to the separation of signal frequencies in the time domain is desirable to give resolution in the frequency domain.

2.3.4 Sample Spinning

Sample spinning about an axis inclined to the B_0 field is employed in many SSNMR experiments. It is used to remove line broadening from various interactions that include a Legendre term of the form $P_2^0 = 3\cos^2(\theta_n) - 1$. Consider the dipolar interaction as an example. The first order terms in the Hamiltonian are of such a form. θ_n is defined to be the angle between the B_0 field which is directed along the z-axis in the laboratory frame and the internuclear vector \mathbf{r} . The angle between the z-axis and the rotation axis is θ_r , θ_{rn} is the angle between the axis of rotation and the internuclear vector, and ωt is the rotation angle about the rotation axis. The cosine addition theorem for this geometry gives [14, 37]

$$\cos(\theta_n) = \cos(\theta_{rn})\cos(\theta_r) + \sin(\theta_{rn})\sin(\theta_r)\cos(\omega t) \quad (2.52)$$

Generalizing with the unnormalized addition theorem for Legendre polynomials, including the rotation,

$$P_2^0(\cos(\theta_n)) = \sum_{m=-l}^l P_l^m(\cos(\theta_r))P_l^m(\cos(\theta_{rn}))e^{im\omega t} \quad (2.53)$$

and taking the real part

$$3\cos^2(\theta_n) - 1 = (3\cos^2(\theta_r) - 1)(3\cos^2(\theta_{rn}) - 1) + \sin(2\theta_r)\sin(2\theta_{rn})\cos(\omega t) + \sin^2(\theta_r)\sin^2(\theta_{rn})\cos(2\omega t) \quad (2.54)$$

$$(2.55)$$

This last equation shows that if $\theta_r = \cos^{-1}(1/\sqrt{3})$, then the first term drops out. This choice of angle is referred to as the “magic” angle. The second and third terms give rise in the spectrum to what are called spinning sidebands [14]. Figure 2.4 gives the static spectrum of the nitrogen in a sample of glycine. 2.5 shows the spinning sidebands for the nitrogen in a sample of glycine. The sample was spun at 5 kHz. Sidebands appear at the spinning frequency, ω . Spinning frequency is usually set to remove broadening in the spectrum from the spin interactions. For complete removal of broadening the spinning speed is set to the spectral breadth of the interaction.

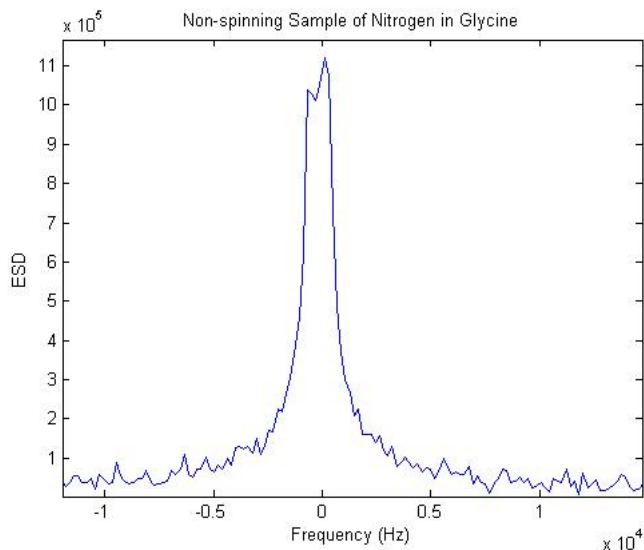


Figure 2.4: Spinning sidebands in the spectrum of ^{15}N in glycine.

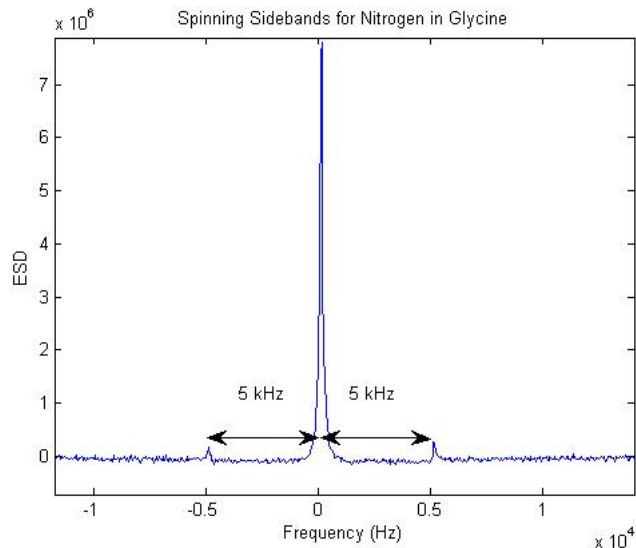


Figure 2.5: Spinning sidebands in the spectrum of ^{15}N in glycine.

2.4 Spin Interactions

When the Zeeman field is applied to an atom or molecule, the nucleus experiences a field different in magnitude from the Zeeman field. The effect comes from the total angular momentum of electrons surrounding the nucleus. This effect is termed electronic, or chemical, shielding. The orbital as well as spin angular momentum of electrons gives rise to an interaction termed scalar coupling. Dipole moments of the nuclear spins interact through the dipolar coupling. Nuclei which exhibit a quadrupole moment interact with the electric field gradient from the electron cloud. An overview of the interactions is given in Table 2.1.

2.4.1 Chemical Shielding

The Hamiltonian describing chemical shielding for a single nucleus can be expressed in Cartesian tensors as

$$\mathcal{H}_{CS} = \gamma \mathbf{I} \cdot \boldsymbol{\sigma} \cdot \mathbf{B} \quad (2.56)$$

Table 2.1: Spin interactions in SSNMR. Abbreviations are μ_N : nuclear dipole moment, B_0 : external magnetic field, L : electron orbital angular momentum, Q : nuclear quadrupole moment, EFG: electron cloud electric field gradient.

Interaction	Physical Origin	Effect on Spectrum	Relative Magnitude
Zeeman	μ_N, B_0	Single resonant frequency	1
Chemical Shielding	L, B_0	Frequency shift and broadening	10^{-4} - 10^{-2}
J-Coupling	μ_N, L	Frequency shift and broadening	10^{-5}
Dipolar	μ_N	Broadening	10^{-4} - 10^{-2}
Quadrupolar	Q, EFG	Broadening	10^{-4} - 10^{-1}

σ is a second rank chemical shift tensor that describes the effect of electron orbitals on the static \mathbf{B} field at the nucleus. The isotropic value, principal value and asymmetry parameters in terms of the PAS components of σ are

$$R = \frac{1}{3} \text{Tr} \sigma \quad (2.57)$$

$$\delta = \frac{2}{3} (\sigma_{zz} - \frac{1}{2} (\sigma_{xx} + \sigma_{yy})) \quad (2.58)$$

$$\eta = \frac{3\sigma_{yy} - \sigma_{xx}}{2\delta} \quad (2.59)$$

The elements of the chemical shift tensor in the PAS are conventionally labeled with $\sigma_{zz} \geq \sigma_{xx} \geq \sigma_{yy}$. R is called the isotropic chemical shift. $\frac{3}{2}\delta$ is called the chemical shielding anisotropy. η is the chemical shielding asymmetry. In terms of irreducible spherical tensors, \mathcal{H}_{CS} includes components with $l = 0, 1, 2$. In practice, the $l = 0, 2$ components are the only ones considered. $l = 1$ components contribute to T_1 relaxation [38]. No direct spectral observation of the antisymmetric part of the chemical shielding interaction has been performed to date. The zeroth and second rank components directly affect the spectra, and I will use these components to describe the spectral features of chemical

shift. They are given in the Zeeman frame as

$$T_{00} = I_z B_z \quad (2.60)$$

$$T_{20} = \sqrt{\frac{2}{3}} I_z B_z \quad (2.61)$$

$$T_{2\pm 1} = \frac{1}{\sqrt{2}} I^\pm B_z \quad (2.62)$$

To first order, i.e. taking the chemical shift as a perturbation on the Zeeman interaction, only the terms with $m = 0$ survive. The first order Hamiltonian expressed in irreducible spherical tensors in the Zeeman frame

$$\mathcal{H}_{CS} = \gamma T_{00} \rho_{00} + \gamma T_{20} \sum_{m'} \mathcal{D}_{m' -m}^2 \rho_{2m'} \quad (2.63)$$

For a certain orientation of the PAS, this gives a particular frequency. As an example, take the PAS of ρ to be the same as the Zeeman frame

$$\mathcal{H}_{CS} = \gamma T_{00} \rho_{00} + \gamma T_{20} \rho_{20} \quad (2.64)$$

$$= \gamma I_z B_z R + \gamma \sqrt{\frac{2}{3}} (I_z B_z \sqrt{\frac{3}{2}} \delta) \quad (2.65)$$

$$= \gamma B_z I_z \sigma_{zz} \quad (2.66)$$

Thus to first order, a particular orientation of the molecule gives a single frequency added to or subtracted from the Zeeman frequency depending on the sign of σ_{zz} . Several chemically distinct nuclei in a single crystal lattice will each give different frequencies, since their PAS's will not generally coincide.

In the case of powdered crystal, each individual crystallite will be in a different orientation. This produces a range of frequencies for each nucleus which will result in a broad spectrum, called the powder pattern. An example of a powder pattern is given in Figure 2.6. Figure 2.7 shows the same sample with

the powder pattern removed by sample spinning and decoupling. Decoupling will be covered below.

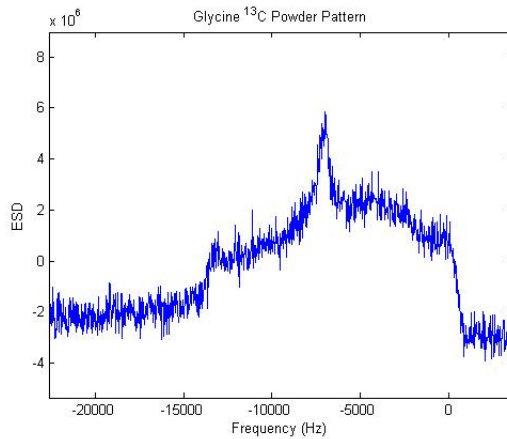


Figure 2.6: Static powder pattern of ^{13}C in glycine. Data was taken on a 9.4 T magnet. The vertical axis is the magnitude squared of the Fourier transform of the time domain signal. Note the breadth of the spectrum ≈ 14 kHz.

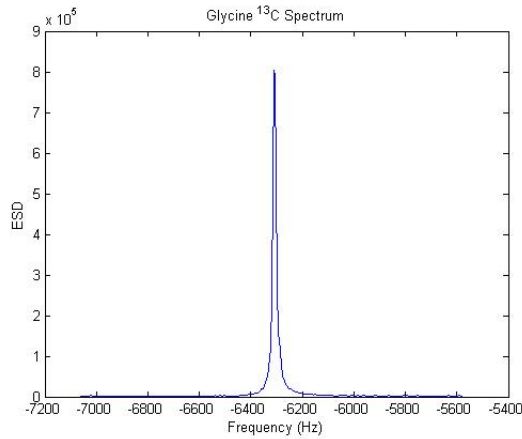


Figure 2.7: Spectrum of ^{13}C in glycine with the powder pattern removed by sample spinning and decoupling. Data was taken on a 9.4 T magnet. The vertical axis is the magnitude squared of the Fourier transform of the time domain signal. Note the breadth of the spectrum ≈ 100 Hz.

2.4.2 J-Coupling

The scalar, indirect spin-spin, or J-coupling Hamiltonian for two spins labeled by i, k is

$$\mathcal{H}_J = \gamma \mathbf{I}^i \cdot \mathbf{J}^{ik} \cdot \mathbf{I}^k \quad (2.67)$$

It involves spin operators for two nuclei coupled through a second rank J-coupling tensor containing the orbital electron spin details. The term indirect spin-spin comes from the indirect nature of the coupling between nuclear spins through their electronic bond. The isotropic value, principal value and asymmetry parameters in terms of the PAS components of \mathbf{J}^{ik} are defined similarly to the chemical shift parameters.

$$R = \frac{1}{3} \text{Tr} \mathbf{J} \quad (2.68)$$

$$\delta = \frac{2}{3} (J_{zz} - \frac{1}{2} (J_{xx} + J_{yy})) \quad (2.69)$$

$$\eta = \frac{3}{2} \frac{J_{yy} - J_{xx}}{\delta} \quad (2.70)$$

R is called the scalar coupling constant, δ the scalar coupling anisotropy, and η the scalar coupling asymmetry parameter. As with the chemical shielding tensor, the scalar coupling tensor includes components with $l = 0, 1, 2$. The isotropic and symmetric components can be measured [21]. The antisymmetric contributions have not been either directly or indirectly measured to date [23].

\mathbf{J} includes contributions from several distinct electron-nucleus couplings. These include diamagnetic and paramagnetic spin orbit, Fermi contact, and spin-dipole couplings. The Fermi contact term comes from the non-zero probability that the electron is located in the same place as the nucleus. It only contributes to the $l = 0$ component of J tensor [21]. The other three couplings

contribute to all components of the tensor. The largest contributors are the Fermi contact and paramagnetic couplings, although these only contribute in second order [21].

2.4.3 Dipolar Coupling

The dipolar interaction Hamiltonian for two spins is given by

$$\mathcal{H}_D = -\frac{\mu_0}{4\pi} \frac{\boldsymbol{\mu}_1 \cdot \boldsymbol{\mu}_2}{r_{12}^3} - \frac{3(\boldsymbol{\mu}_1 \cdot \mathbf{r}_{12})(\boldsymbol{\mu}_2 \cdot \mathbf{r}_{12})}{r_{12}^5} \quad (2.71)$$

$$= -\frac{\mu_0}{4\pi} \frac{\gamma_1 \gamma_2 \hbar^2}{r_{12}^3} (I_1 \cdot I_2 - \frac{3(I_1 \cdot \mathbf{r}_{12})(I_2 \cdot \mathbf{r}_{12})}{r_{12}^2}) \quad (2.72)$$

Here \mathbf{r}_{12} is the vector from nucleus 1 to nucleus 2. The parameter for this interaction is

$$\delta = r_{12} \quad (2.73)$$

Both R and η are zero for dipolar coupled spins. The multiplicative constant divided by \hbar in the Hamiltonian

$$C_D = -\frac{\mu_0}{4\pi} \frac{\gamma_1 \gamma_2 \hbar}{r_{12}^3} \quad (2.74)$$

is termed the dipole coupling constant and gives the maximum frequency range involved for a given inter-nuclear distance. C_D will be used below to determine internuclear distances.

In terms of tensors, there is no antisymmetric component of the \mathbf{D} tensor. This can be seen by inspection of Equation 2.72, since it involves only dot products of vectors. The simplicity of the spatial part of the Hamiltonian makes it useful for determining the distances between nuclei in a sample. The first order terms for a heteronuclear, \mathcal{H}_{HtD} , and homonuclear, \mathcal{H}_{HmD} , dipole

coupling are

$$\mathcal{H}_{HtD} = -\frac{\mu_0}{4\pi} \frac{\gamma_1 \gamma_2 \hbar^2}{r_{12}^3} I_{1z} I_{2z} (3 \cos^2 \theta - 1) \quad (2.75)$$

$$\mathcal{H}_{HmD} = -\frac{\mu_0}{4\pi} \frac{\gamma_1 \gamma_2 \hbar^2}{r_{12}^3} \left(I_{1z} I_{2z} - \frac{1}{4} (I_1^+ I_2^- + I_1^- I_2^+) \right) (3 \cos^2 \theta - 1) \quad (2.76)$$

θ is the angle between the z-axis and the internuclear vector \mathbf{r}_{12} . These terms can be experimentally eliminated by off-resonance excitation as will be shown below.

2.4.4 Quadrupolar Hamiltonian

In terms of constants, spin operators, and parameters, the Quadrupolar Hamiltonian is

$$\mathcal{H}_Q = \frac{e^2 q Q}{4I(2I-1)} \left((3I_z^2 - I^2) + \eta(I_x^2 - I_y^2) \right) \quad (2.77)$$

Where

$$\delta = V_{zz} \equiv eq \quad (2.78)$$

$$\eta = \frac{V_{xx} - V_{yy}}{V_{zz}} \quad (2.79)$$

\mathbf{V} is the electric field gradient (EFG) tensor. Like the dipolar tensor, \mathbf{V} is completely symmetric, thus there are no $l = 0, 1$ components. The charge of the electron is e , and eQ is defined as the quadrupole moment. The Quadrupole interaction is very sensitive to the local environment of the nucleus. It also results in a very broad spectrum, since the electrostatic coupling to the electrons provides a relatively fast mechanism for T_2 relaxation.

2.5 The Density Matrix

Given an ensemble of systems with the state of the k th system,

$\Psi_k(t) = \sum_k c_{ik}(t)|i\rangle$, occurring with probability $p_k(t)$, the expectation value of an operator, A , is of interest.

$$\langle A \rangle = \sum_k p_k(t) \langle \Psi_k(t) | A | \Psi_k(t) \rangle \quad (2.80)$$

$$= \sum_{i,j,k} p_k(t) c_{ik}(t) c_{jk}^*(t) \langle j | A | i \rangle \quad (2.81)$$

$$= \sum_{i,j} \rho_{ij}(t) A_{ji} = Tr(A\rho(t)) \quad (2.82)$$

In the last equation, Tr stands for trace of a matrix and $\rho(t)$ is the density operator. This operator is defined as [27]

$$\rho(t) = \sum_k p_k |\Psi_k(t)\rangle \langle \Psi_k(t)| \quad (2.83)$$

$$= \sum_{i,j,k} p_k c_{ik} c_{jk}^* |i\rangle \langle j| \quad (2.84)$$

$$= \sum_{i,j} \overline{c_{ik} c_{jk}^*} |i\rangle \langle j| \quad (2.85)$$

Since we are dealing with an ensemble, $\overline{c_{ik} c_{jk}^*}$ is the ensemble average of the complex amplitudes of the eigenstates. The matrix elements of $\rho(t)$ are

$$\langle n | \rho(t) | m \rangle = \rho_{nm}(t) = \overline{c_{nk}(t) c_{mk}^*(t)} \quad (2.86)$$

We see that the diagonal elements of the density matrix are probabilities. These elements correspond to ensemble populations of the eigenstates composing Ψ . So $Tr(\rho(t)) = 1$ since all nuclei in the ensemble must be in one of the eigenstates composing Ψ . The off-diagonal elements give coherent su-

perpositions of eigenstates. These coherent superpositions are simply called “coherence” [34].

Since the density matrix is a function of time, we would like to know how it changes with time. We can determine its equation of motion by first considering the Schroedinger equation for $\Psi(t) = \sum_i c_i(t)|i\rangle$,

$$i\hbar \sum_i \frac{dc_i}{dt} |i\rangle = \sum_i c_i \hat{H} |i\rangle \quad (2.87)$$

Operating on this equation from the left with $\langle l|$ gives two equations, one the complex conjugate of the other

$$i\hbar \frac{dc_l}{dt} = \sum_i H_{li} c_i \quad (2.88)$$

$$-i\hbar \frac{dc_l^*}{dt} = \sum_i H_{li}^* c_i^* \quad (2.89)$$

Using these and the definition of $\rho(t)$,

$$i\hbar \frac{d\rho_{nm}}{dt} = i\hbar \frac{dc_n c_m^*}{dt} \quad (2.90)$$

$$= i\hbar \left(\frac{dc_n}{dt} c_m^* + c_n \frac{dc_m^*}{dt} \right) \quad (2.91)$$

$$= i\hbar \sum_i (c_i H_{ni} c_m^* - c_n c_i^* H_{mi}^*) \quad (2.92)$$

$$= \sum_i (H_{ni} \rho_{im} - \rho_{ni} H_{im}) \quad (2.93)$$

In operator form,

$$i\hbar \frac{d\rho}{dt} = [\hat{H}, \rho] \quad (2.94)$$

This equation is called the Liouville-von Neumann equation. It is a surrogate for the Schroedinger equation, and the density operator becomes a surrogate

for the wave function. In equilibrium, $\frac{d\rho}{dt} = 0$. So ρ commutes with \hat{H} and is therefore diagonal in the eigenbasis of \hat{H} .

Looked at in a different way,

$$\rho_{nm} = \overline{c_n c_m^*} = \overline{|c_m| |c_n| e^{i(\alpha_n - \alpha_m)}} \quad (2.95)$$

and in equilibrium it is assumed that α_m and α_n are uniformly distributed. This is the hypothesis of random phases and implies that there are no coherent states[10]. With this assumption the average value of ρ_{nm} vanishes for all values of $n \neq m$. Hence the matrix is diagonal.

In equilibrium,

$$\rho = \frac{e^{-\frac{\hat{H}}{kT}}}{Z} \quad (2.96)$$

where $Z = Tr(e^{-\frac{\hat{H}}{kT}}) = \sum_E e^{-\frac{E}{kT}}$ is the partition function of the system [36]. To determine the populations in each state, we look at our model spin $\frac{1}{2}$ system. Since the E values are small compared to kT , $\frac{\gamma \hbar I B}{kT} \approx 10^{-6}$, we can expand the exponential, keeping only the first two terms. The populations are

$$n_i = \frac{1 - \frac{E_i}{kT}}{\sum_m 1 - \frac{E_i}{kT}} \quad (2.97)$$

$$= \frac{1}{2} \left(1 - \frac{E_i}{kT}\right) \quad (2.98)$$

For the equilibrium density matrix,

$$\rho = \frac{1}{2} \begin{pmatrix} 1 - \frac{E_1}{kT} & 0 \\ 0 & 1 - \frac{E_2}{kT} \end{pmatrix} \quad (2.99)$$

$$= \frac{1}{2} \begin{pmatrix} 1 & 0 \\ 0 & 1 \end{pmatrix} + \frac{1}{2} \begin{pmatrix} -\frac{E_1}{kT} & 0 \\ 0 & -\frac{E_2}{kT} \end{pmatrix} \quad (2.100)$$

$$= \frac{1}{2} \begin{pmatrix} 1 & 0 \\ 0 & 1 \end{pmatrix} + \frac{1}{2} \begin{pmatrix} p_{pop} & 0 \\ 0 & -p_{pop} \end{pmatrix} \quad (2.101)$$

where $p_{pop} = \frac{\gamma \hbar B}{2kT}$ for a spin $\frac{1}{2}$ system. When working with the density matrix, the second matrix term is of most importance since it gives the population difference, since the first term is a constant matrix. Population difference is what gives rise to magnetization and an observable signal. The matrix containing this information is termed the partial or magnetization density matrix [49]. The partial density matrix has a trace of 0, while the trace of the full density matrix is equal to 1. We will be using the partial density matrix almost exclusively when dealing with what follows, and reference to the density matrix will be understood to be the partial density matrix.

2.5.1 Creation of Quantum Coherence

As noted above, coherence is created by producing non-zero off-diagonal elements in the density matrix. This is accomplished by operating on the density matrix with rotation matrices. Experimentally, this is equivalent to applying pulses to the sample. We will continue with the example of a single spin $\frac{1}{2}$ nuclear system.

Rotation operators take the form,

$$\widehat{R}_{\phi\hat{\mathbf{n}}} = e^{-i\phi\hat{\mathbf{n}}\cdot\hat{I}} \quad (2.102)$$

where $\hat{\mathbf{n}}$ is a unit vector in an arbitrary direction which defines the axis about which rotation is taking place. The form of the spin $\frac{1}{2}$ matrix operator in the I_z basis for a rotation about the x-axis is

$$\widehat{R}_{\phi\hat{\mathbf{x}}} = \begin{pmatrix} \cos(\phi/2) & -i \sin(\phi/2) \\ -i \sin(\phi/2) & \cos(\phi/2) \end{pmatrix} \quad (2.103)$$

The effect of a 90 degree x pulse on the equilibrium density matrix is

$$\rho = \widehat{R}_{90x}\rho_{eq}\widehat{R}_{90x}^{-1} \quad (2.104)$$

$$= \frac{p_{pop}}{4} \begin{pmatrix} 1 & -i \\ -i & 1 \end{pmatrix} \begin{pmatrix} 1 & 0 \\ 0 & -1 \end{pmatrix} \begin{pmatrix} 1 & i \\ i & 1 \end{pmatrix} \quad (2.105)$$

$$= \frac{p_{pop}}{2} \begin{pmatrix} 0 & i \\ -i & 0 \end{pmatrix} \quad (2.106)$$

This shows that populations have been equalized and there are off-diagonal terms, or coherences, that have been created. Looking at the expectation value of I_x after the pulse,

$$\langle I_x \rangle = Tr(I_x\rho) \quad (2.107)$$

$$= Tr\left(\frac{I^+ + I^-}{2}\rho\right) \quad (2.108)$$

$$= Tr\left(\frac{p_{pop}}{4} \left(\begin{pmatrix} 0 & 1 \\ 0 & 0 \end{pmatrix} + \begin{pmatrix} 0 & 0 \\ 1 & 0 \end{pmatrix} \right) \begin{pmatrix} 0 & i \\ -i & 0 \end{pmatrix} \right) \quad (2.109)$$

$$= 0 \quad (2.110)$$

Whereas using the Pauli spin matrix, σ_y , $\langle I_y \rangle$ is

$$\langle I_y \rangle = Tr(I_y \rho) \quad (2.111)$$

$$= Tr\left(\frac{\sigma_y}{2} \rho\right) \quad (2.112)$$

$$= Tr\left(\frac{p_{pop}}{4} \begin{pmatrix} 0 & -i \\ i & 0 \end{pmatrix} \begin{pmatrix} 0 & i \\ -i & 0 \end{pmatrix}\right) \quad (2.113)$$

$$= -\frac{p_{pop}}{2} \quad (2.114)$$

In this case, we have a non-zero expectation value signifying that magnetization lies along the y axis. The direction of this magnetization depends on the sign of p_{pop} .

Spin systems with only two states give rise to single quantum coherence. For spin systems with more than two states, there are possibilities for more than single quantum coherence. As stated above, coherence between states $|r\rangle$ and $|s\rangle$ is given by a non-zero matrix element ρ_{rs} . A coherence order p , or p -quantum coherence, is associated with states $|r\rangle$ and $|s\rangle$ as [27]

$$p = \langle r | \sum_i I_{zi} | r \rangle - \langle s | \sum_i I_{zi} | s \rangle \quad (2.115)$$

$$= M_r - M_s \quad (2.116)$$

In the last equation, M_n is the total magnetic quantum number for state n .

Of particular importance are rotations of the density matrix about the

z-axis. Consider one component of the density operator,

$$\widehat{R}_{\phi z} \rho_{rs} \widehat{R}_{\phi z}^{-1} = e^{-i\phi \hat{I}_z} c_{rs} |r\rangle \langle s| e^{i\phi \hat{I}_z} \quad (2.117)$$

$$= e^{-i\phi M_r} c_{rs} |r\rangle \langle s| e^{i\phi M_s} \quad (2.118)$$

$$= c_{rs} |r\rangle \langle s| e^{-i\phi p_{rs}} \quad (2.119)$$

$$= \rho_{rs} e^{-i\phi p_{rs}} \quad (2.120)$$

So rotations about z give phase changes in the density matrix that depend on coherence order. This will be important for the detection of various orders of coherence.

Transformation properties of multiple quantum coherence can be expressed more succinctly with irreducible tensor operators. The rotation matrices can be decomposed in terms of Euler angles,

$$R(\alpha, \beta, \gamma) = e^{-i\alpha I_z} e^{-i\beta I_y} e^{-i\gamma I_z} \quad (2.121)$$

For transformations, schematic notation is effective,

$$T_{lm} \xrightarrow{\gamma I_z} \xrightarrow{\beta I_y} \xrightarrow{\alpha I_z} \sum_{m'=-l}^l T_{lm} \mathcal{D}_{m'm}^{(l)}(\alpha, \beta, \gamma) \quad (2.122)$$

The spin density matrix written in terms of irreducible tensors is [34, 6]

$$\rho = \sum_{l,m} b_{lm} T_{lm} \quad (2.123)$$

Here $m = -l, \dots, l$ can be identified with the coherence order and l is the tensor rank. The b_{lm} are the weighting coefficients for the various elements of

the density matrix. Under a rotation about the z-axis,

$$T_{lm} \xrightarrow{\phi I_z} T_{lm} e^{-im\phi} \quad (2.124)$$

For a rotation about the y axis,

$$T_{lm} \xrightarrow{\phi I_y} \sum_{m'=-l}^l T_{lm}^{(k)} \mathcal{D}_{m'm}^{(l)}(\phi) \quad (2.125)$$

Finally under free precession,

$$T_{lm} \xrightarrow{\mathcal{H}t} \sum_{k',l'} b_{l'm}^{(k')} T_{l'm}^{(k')} \quad (2.126)$$

Various quantum coherence orders are accessed by combinations of rotations via pulses and free precession. Note that in these cases, the system is not in equilibrium any longer, so the phases are not random. In particular, rotations about axes transverse to the static field will provide various orders of coherence within the current rank of the operator. Free precession under the Hamiltonian will change the rank and therefore accessible coherence orders. Utilizing these transformations of spin to perform multiple quantum experiments is the topic of the next section.

2.5.2 Detection of Quantum Coherence

Only single quantum coherence can be observed, since the observable in NMR is $\langle I_x \rangle \propto Tr(I_x \rho)$. For a general ρ , I_x picks out non-zero elements ρ_{rs} where $r - s = \pm 1$. Thus, information carried by higher orders needs to be transferred to the orders with $\Delta M = p = \pm 1$. Coherence transfer accomplishes this [27]. Coherence transfer occurs between the different state transitions of the system. To see this, we use Equations 2.123, 2.124, and 2.125 and focus on a particular

order of the density operator, ρ^p . Under the transformation of Equation 2.124,

$$\rho^p \xrightarrow{\phi \hat{I}_z} \rho^p e^{-ip\phi} \quad (2.127)$$

For an operator that is transformed by a rotation of ϕ about the z-axis,

$$O(\phi) = R_z(\phi) O R_z^{-1}(\phi) \quad (2.128)$$

$$= e^{-i\phi \hat{I}_z} O e^{i\phi \hat{I}_z} \quad (2.129)$$

and its inverse,

$$O^{-1}(\phi) = R_z(\phi) O^{-1} R_z^{-1}(\phi) \quad (2.130)$$

$$= e^{-i\phi \hat{I}_z} O^{-1} e^{i\phi \hat{I}_z} \quad (2.131)$$

Note the notation: $O^{-1}(\phi)$ is the rotated inverse of the operator O . Operating with this on the p_0 -order density operator,

$$O(\phi) \rho_0^p O^{-1}(\phi) = e^{-i\phi \hat{I}_z} O e^{i\phi \hat{I}_z} \rho_0^p e^{-i\phi \hat{I}_z} O^{-1} e^{i\phi \hat{I}_z} \quad (2.132)$$

$$= e^{-i\phi \hat{I}_z} O \rho_0^p e^{ip\phi} O^{-1} e^{i\phi \hat{I}_z} \quad (2.133)$$

$$= e^{-i\phi \hat{I}_z} \sum_n \rho^{p_n} e^{i\phi \hat{I}_z} e^{ip_0\phi} \quad (2.134)$$

$$= \sum_n \rho^{p_n} e^{-i(p_n - p_0)\phi} \quad (2.135)$$

This shows that a change in coherence order due to the effect of a rotated operator gives a phase term which corresponds to the change in coherence order and the rotation angle of the operator. For multiple of these operations, the phase terms are carried along. Coherence-phase information will be carried into the observed signal. Since a pulse generally creates multiple coherence

orders, it would be desirable to restrict the coherence transfer pathway to particular changes in order.

To accomplish this, we perform N_i experiments with increments in the phase of the operator. Following the development of Ernst, et al., [34],

$$\phi_i = \frac{k_i 2\pi}{N_i}, \quad k_i = 0, 1, \dots, N_i - 1 \quad (2.136)$$

The detected signal s is a superposition of the N_i experiments,

$$s(t) = \sum_{k_i} s(\phi_i, t) \quad (2.137)$$

Each experiment itself contains a superposition of coherence orders as in Equation 2.135. The coherence order can be appropriately analyzed with a Fourier transform of $s(t)$

$$s(\Delta p_i, t) = \frac{1}{N_i} \sum_{k_i} s(\phi_i, t) e^{i\Delta p_i \phi_i} \quad (2.138)$$

This analysis gives the contribution of coherence order in the detected signal. The N_i experiments select a set of values of coherence orders according to

$$\Delta p_i^{(selected)} = \Delta p_i^{(desired)} \pm n N_i, \quad n = 0, 1, 2, \dots \quad (2.139)$$

This amounts to one pulse in a multi-pulse experiment manipulated to give a set of specific coherence orders [34]. For example, if we desire a change in coherence of $\Delta p^{(desired)} = 1$, and we perform 3 experiments, then the selected changes in coherence are $\Delta p^{(selected)} = \dots, -5, -2, 1, 4, \dots$. This is only a selection for a change in coherence order for one pulse. Obviously, the more experiments which are run for a given observation, the more we isolate our

desired change in coherence order.

A complete multiple quantum experiment can be described by giving a coherence transfer pathway. This description gives the order of coherences that are achieved for all pulses over the course of the experiment. A graphical representation of a coherence transfer pathway for a simple one pulse experiment is given in Figure 2.8.

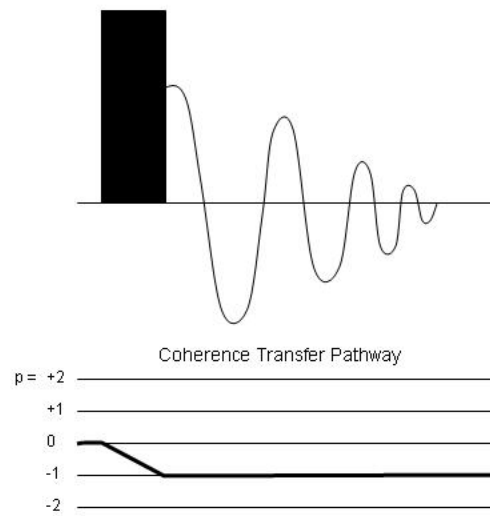


Figure 2.8: Graphical depiction of the coherence transfer pathway for a single pulse.

Chapter 3

The Quantum Coherence

Experiment

Quantum coherence experiments in solids treated here are performed on systems containing nuclei with a spin quantum number $> \frac{1}{2}$. There are also possibilities for creating quantum coherence in spin $\frac{1}{2}$ systems [47]. However this work will deal only with quadrupolar nuclei. Quantum coherence experiments were developed to reduce the spectral breadth of quadrupolar interactions. Experiments utilizing coherence transfer pathways that are symmetric about the central energy states are termed multiple quantum magic angle spinning (MQMAS) experiments. Experiments utilizing quantum coherence about energy levels which are not symmetric about the central energy states are termed satellite transition magic angle spinning (STMAS) experiments.

3.1 Perturbation Terms in The Quadrupolar Hamiltonian

A perturbation expansion of the quadrupolar Hamiltonian given by Trebosc, et al. [20], written in terms of frequency differences of energy levels is useful for pointing out important features of multiple quantum experiments

$$\nu_{m,n}^{(1)} = \frac{\nu_Q(m^2 - n^2)}{4}(3 \cos \beta_R^2 - 1)d_{00}^2(\chi) \quad (3.1)$$

$$\begin{aligned} \nu_{m,n}^{(2)} = & \frac{\nu_Q^2}{5040\nu_0}(-168[m(S(S+1) - 3m^2) - n(S(S+1) - 3n^2)] \\ & - 60[m(8S(S+1) - 12m^2 - 3) - n(8S(S+1) - 12n^2 - 3)]d_{00}^2(\chi)d_{00}^2(\beta_R) \\ & + 36[m(18S(S+1) - 34m^2 - 5) - n(18S(S+1) - 34n^2 - 5)]d_{00}^4(\chi)d_{00}^4(\beta_R) \end{aligned} \quad (3.2)$$

where $\eta = 0$ see note on this below, m and n are the z-components for the states of total nuclear spin S , β_R is the angle relating the quadrupolar PAS to the sample rotation frame, χ is the angle between the static \mathbf{B} and the sample rotation frame, $\nu_Q = \frac{3e^2qQ}{2S(2S-1)}$ is the quadrupole characteristic frequency, and ν_0 is the Larmor frequency of the nucleus. Taking $\eta = 0$ applies to situations where the EFG is symmetric about the transverse PAS coordinates. Symmetric crystal structures give η values very close to zero [10]. In this work, I look at SiO₂ crystals with tetrahedral symmetry which makes this assumption valid.

The expansion above shows a couple of important spectral characteristics. First, for rotation about the magic angle, $d_{00}^2(\chi) = (3 \cos \theta_m^2 - 1)/2 = 0$. These terms drop out for sample spinning. Second, for $|m| = |n|$ the first order term drops out. For spinning at an appropriate angle, $d_{00}^4(\chi) = (35 \cos \chi^4 - 30 \cos \chi^2 + 3)/8 = 0$. However no rotation about a single angle will give $d_{00}^4(\chi) = d_{00}^2(\chi) = 0$. Reduction of the $d_{00}^4(\chi)$ term in second order is the

objective of performing quantum coherence experiments.

3.2 Satellite Transitions

Depending on the spin system, multiple satellite transitions are available. Figure 3.1 gives an energy level diagram for a spin $\frac{5}{2}$ nucleus with the various possible single quantum satellite transitions. Populations of the states in a system of spins follows a Boltzmann distribution. Lowest energy states will have the

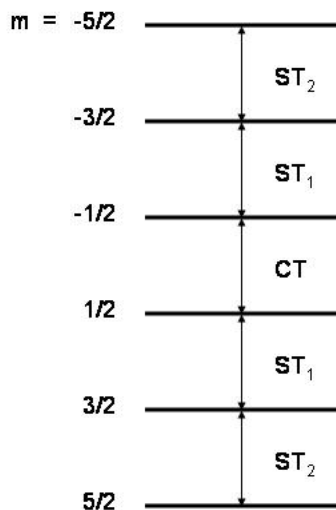


Figure 3.1: Energy level diagram for a spin $\frac{5}{2}$ nucleus. CT is the central transition. ST_n in the nth satellite transition.

highest populations and thus the largest magnetization. STMAS experiments take advantage of this, transferring magnetization through coherence between the satellite transitions. Ideally, the largest and smallest population magnetizations are transferred to the central transition (CT).

3.2.1 Satellite Transition Experiment

The pulse sequence and coherence transfer pathway for a single quantum STMAS (1QSTMAS) experiment is shown in Figure 3.2. The phases ϕ_i are

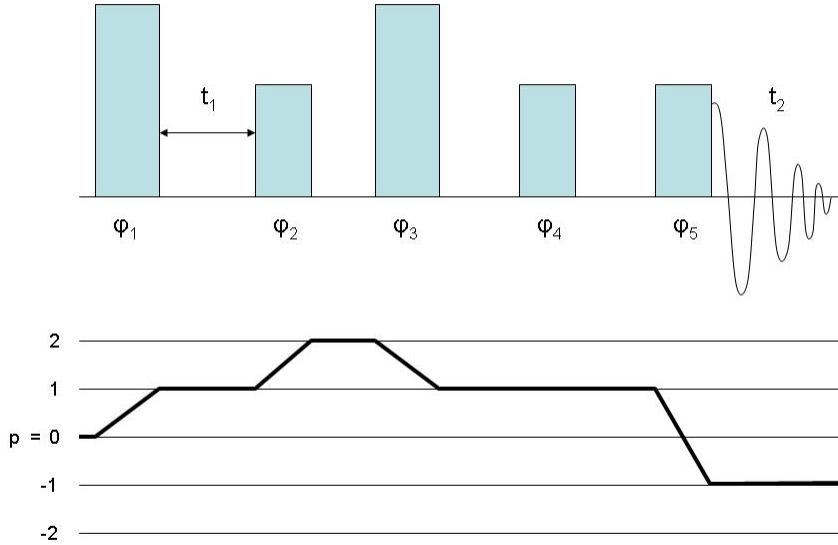


Figure 3.2: The 1QSTMAS pulse sequence and coherence transfer pathway. The ϕ_i are the pulse phases about the z-axis. The t_1 variable is incremented to give a 2-dimensional spectrum.

determined using the Equations 2.132 and 2.139. To ensure the desired coherence order pathway during observation, the phase of the receiver is also cycled according to [34]

$$\phi_R = - \sum \Delta p_i \phi_i \quad (3.3)$$

For a 1QSTMAS pulse sequence with 4 phases for the first, second, and fifth pulses keeping the third and fourth pulses at a constant phase, to attain one complete signal, the sequence must be performed 4^3 times.

The observed signal is 2-dimensional

$$s(t_1, t_2) \propto e^{-i\nu^{(2)}_{\pm\frac{3}{2}, \pm\frac{1}{2}} t_1} e^{-i\nu^{(2)}_{-\frac{1}{2}, +\frac{1}{2}} t_2} \quad (3.4)$$

The form of the second order term in Equation 3.2 involves two terms, assuming magic angle spinning. The first term is a constant. The second term gives the fourth order broadening. It is the second term that multiple quantum experiments seek to remove. As seen in the 2-dimensional signal, appropriate choices of t_2 given a t_1 will result in only a constant exponential term. This “refocusing” of the signal to remove second order broadening is the means by which multiple quantum experiments attain spectra with resolution in the second dimension.

Figure 3.3 is a schematic representation of possible results from a 1QSTMAS experiment performed on a spin $\frac{5}{2}$ nucleus. Generally, results include contributions from the various transitions. According to Figure 3.1, these contributions come from the CT, ST₁, and ST₂ transitions. The slopes of the lines in the spectrum are calculated as the ratio, R , of second order quadrupolar broadenings of the transitions involved. Thus $R = 1$ for CT-CT, $R = 7/24$ for ST₁-CT, and $R = -11/6$ for ST₂-CT [56, 46]. The spectrum is typically sheared according to the R to give the isotropic spectrum in the F_1 dimension [45]. Figure 3.4 shows the effect of shearing for the ST₁-CT portion to give an isotropic projection on the F_1 axis. Results of the 1QSTMAS experiment for ¹⁷O in silica are presented in the next section.

3.3 Results of Silica Phase Cycling STMAS

The first multiple quantum experiment (MQMAS) was performed in 1995 by Frydman and Harwood [24]. In 2000, Gan established the STMAS experiment

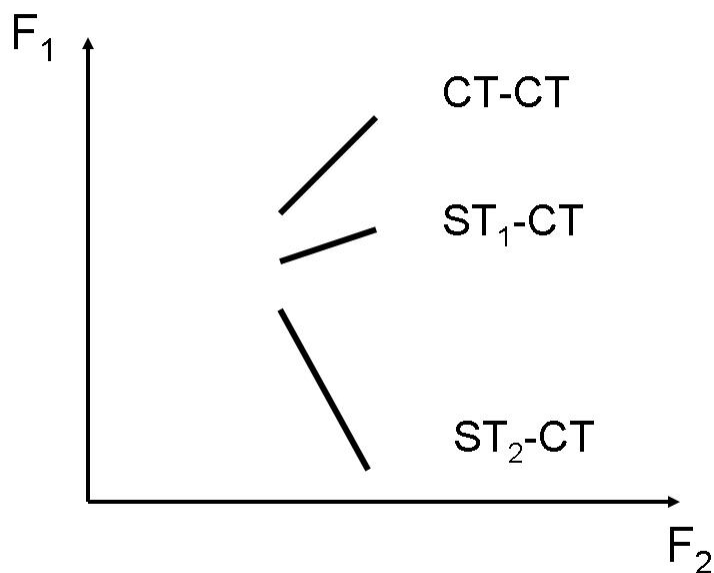


Figure 3.3: Schematic of possible results from a 1QSTMAS experiment performed on a spin $\frac{5}{2}$ nucleus. F_1 and F_2 are the Fourier transformed t_1 and t_2 dimensions. The slope of lines in the spectrum are calculated as the ratio, R , of second order rank 4 broadenings of the transitions involved. Thus $R = 1$ for CT-CT, $R = 7/24$ for ST₁-CT, and $R = -11/6$ for ST₂-CT.

[55]. Although STMAS provides enhanced sensitivity over MQMAS, it has not attracted the same level of interest [44]. Hajjar et al. have studied the effects of phase cycling in MQMAS experiments [35]. There have not been any studies in the phase cycling effects on STMAS experiments. I present results of phase cycling investigations here.

Phase cycling STMAS experiments were performed on SiO₂ enriched to 10% ¹⁷O. The sample was graciously provided by Marek Pruski at Iowa State University. All experiments were performed on a 14.09 T magnet with a 3.2 mm probe and 10 kHz sample spinning. Spectra have been referenced to the frequency of 81.312792 MHz. The theory presented in Equation 2.139 implies that phase cycling of the individual pulses influences the change in coherence

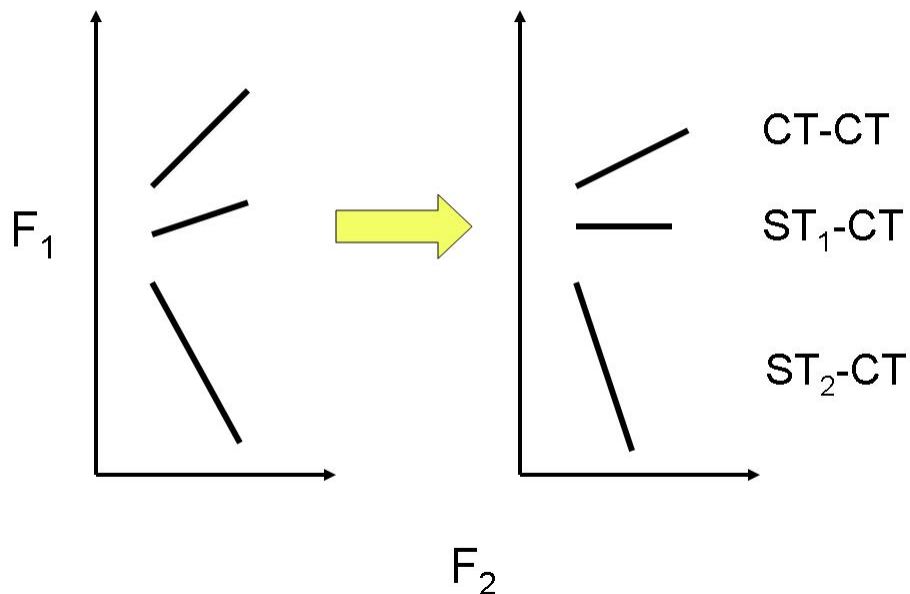


Figure 3.4: Shearing of STMAS spectrum. The spectrum has been rotated so that the ST–1-CT portion gives the isotropic projection on the F_1 axis.

orders available in an experiment. Selection of the coherence transfer pathway is determined by Equation 3.3. The objective is to test whether phase cycling influences coherence orders in the spectrum. A 1QSTMAS experiment was implemented varying the phase of the first, second, and fifth pulses in the pulse sequence shown in Figure 3.2. In this implementation of the pulse sequence, the third pulse is not phase cycled and the fourth pulse does not give a change in coherence order by Equation 3.3. All spectra presented have been sheared to give the ST_1 -CT isotropic along the F_1 axis, unless otherwise stated.

Figure 3.5 is a contour plot of the result of a 1QSTMAS experiment performed with 4 phases each for the first, second, and fifth pulses. This phase cycling will be considered the standard phase cycling. Figures 3.6 and 3.7 give the projections along the F_2 and F_1 dimensions. The F_2 projection is the spectrum obtained with a reduction in first order broadening from sample

spinning. Second order broadening is still present, resulting in what appears to be two peaks in the spectrum. The F_1 dimension shows a narrowing of the spectrum from reduction of the second order broadening using the ST_1 -CT coherences.

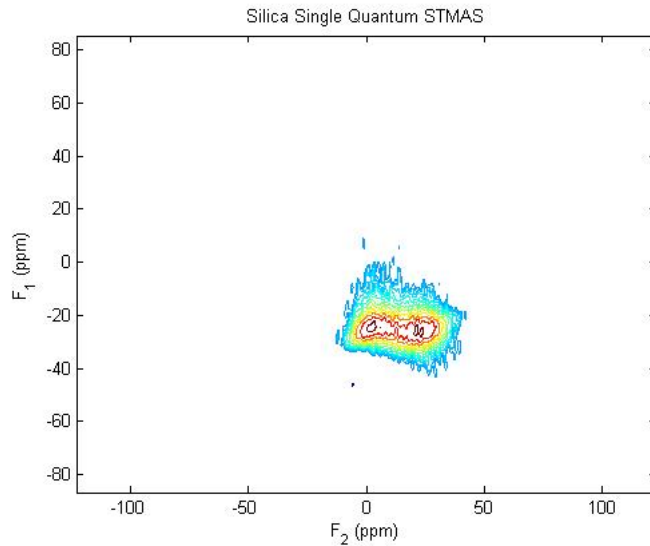


Figure 3.5: The 1QSTMAS spectra of ^{17}O in 10% enriched SiO_2 . Experiments were performed on a 14.09 T magnet.

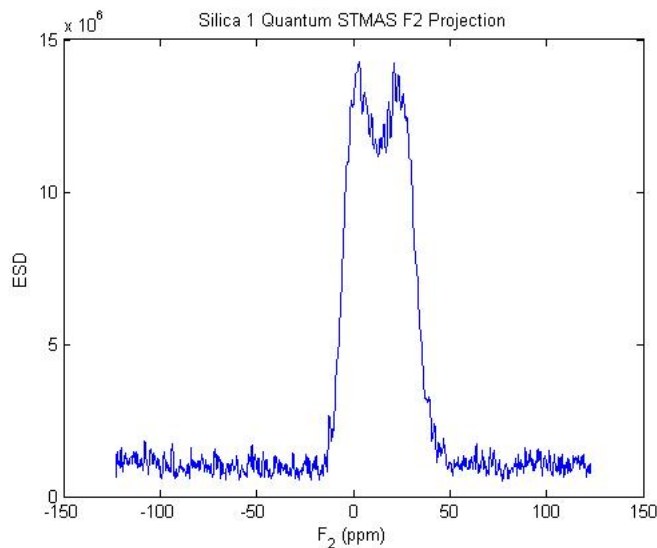


Figure 3.6: The projection of Figure 3.5 along the F_2 axis.

The phase cycle of ϕ_5 was varied by 1, 2, 4, or 8 phases while phases

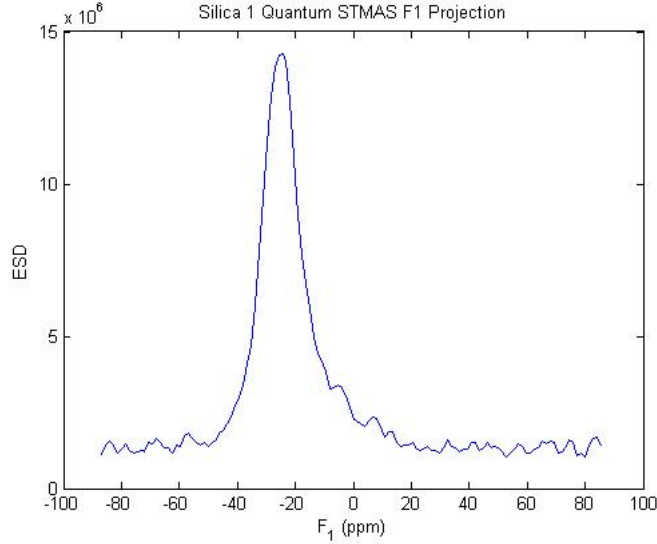


Figure 3.7: The projection of Figure 3.5 along the F_1 axis.

were cycled normally for all other pulses. The spectral width in F_2 is 100 kHz while that in F_1 is 10 kHz. For each phase, I performed the experiment twice. Once with the number of acquisitions constant across phase changes (the number of complete phase cycles varied across phase changes), and once with the number of complete phase cycles constant across phase changes (the number of acquisitions varied across phase changes). The metrics used for comparison are the total two-dimensional integrated area of the spectrum and the full width at half max (FWHM) of the F_1 projection. The results are summarized in Table 3.1.

Table 3.1: Results of the phase cycling experiment for 1QSTMAS on silica.

Number ϕ_5 Phases	32 Complete Phase Cycles		512 complete acquisitions	
	Integral ($\times 10^{10}$)	FWHM (ppm)	Integral ($\times 10^{10}$)	FWHM (ppm)
8	11.9 ± 0.0000017	14.24 ± 0.018	1.47 ± 0.00000447	14.92 ± 0.025
4	5.85 ± 0.00000218	12.89 ± 0.021	1.52 ± 0.00000417	13.49 ± 0.023
2	3.01 ± 0.00000310	12.89 ± 0.02	1.41 ± 0.00000433	14.92 ± 0.021
1	1.53 ± 0.00000431	13.5 ± 0.024	1.52 ± 0.00000421	13.49 ± 0.023

The integrals in the experiments with 32 complete phase cycles show a

trend consistent with the increase in the number of acquisitions defined by the phases. For example, the number of acquisitions for a complete phase cycle with $\phi_5 = 1$ is 16 while for $\phi_5 = 2$ is 32. The number of acquisitions for a complete phase cycle is equal to $N_1 N_2 N_3$ where N_i is the number of phases for the i -th pulse. Thus the integral values double as the number of ϕ_5 phases double. Variation in the FWHM over acquisitions are repeatable, but the reason is not clear. These results generally correspond to those reported in phase cycling in MQMAS experiments [35]. In particular, in STMAS experiments each acquisition adds constructively regardless of phase cycling.

Phase cycling on ϕ_1 and ϕ_2 produced altogether different results. The phase cycle for each was varied by 1 and 2 phases while all other phases were cycled normally. Data for each experiment consist of 32 complete phase cycles. Results for 1 value of ϕ_2 are shown in Figure 3.8. The spectrum shows the appearance of a CT-CT coherence line which does not show up in the 4 phase cycle spectrum. Likewise, Figure 3.9 shows a CT-CT line, though with less

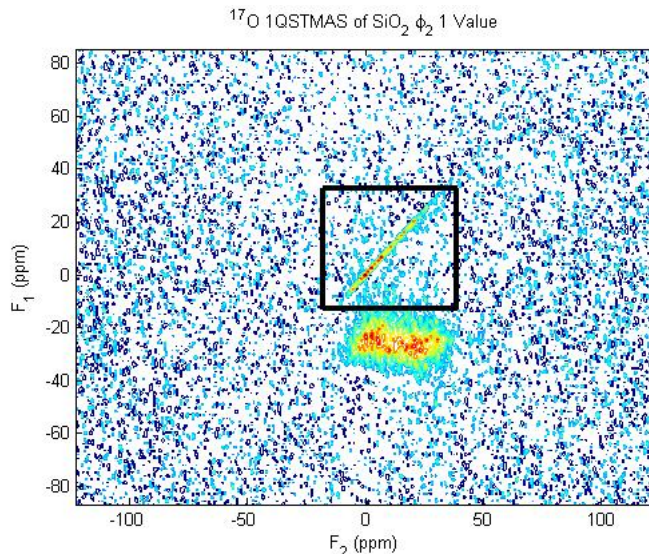


Figure 3.8: The spectrum for one value of ϕ_2 . The boxed area shows a CT-CT line not apparent in the 4 phase cycle spectrum.

magnitude.

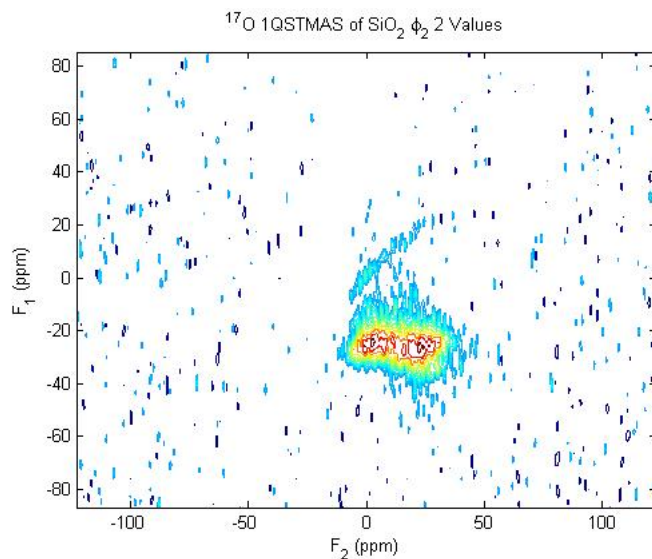


Figure 3.9: The spectrum for two values of ϕ_2 . The CT-CT coherence line is still apparent.

Figures 3.10 and 3.11 show results for ϕ_1 phase cycling of 1 and 2 values, respectively. These spectra show lines that do not appear to correspond

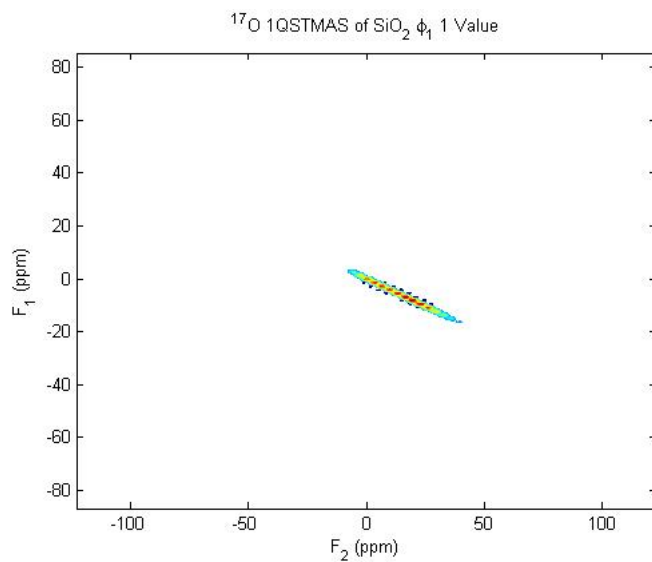


Figure 3.10: The spectrum for one value of ϕ_1 .

to CT-CT, ST_1 -CT, or ST_2 -CT coherences. Furthermore, the spectra appear to be shifted in frequency along the F_1 axis compared to the 4 phase cycle spectrum of Figure 3.6.

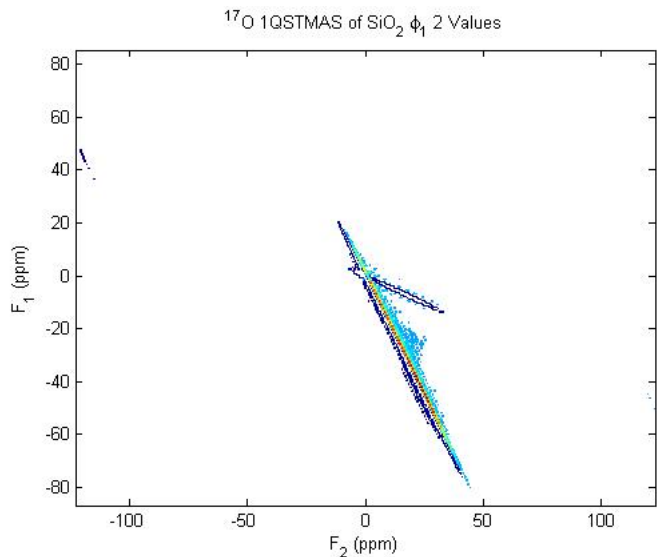


Figure 3.11: The spectrum for two values of ϕ_1 .

Results for phase cycling of the first and second pulses in the 1QSTMAS experiment contrast with results obtained by phase cycling in MQMAS experiments performed by Hajjar, et al. [35]. Experiments performed on the 1QSTMAS experiment in this work show that phase cycling may or may not affect the spectrum. In particular, cycling ϕ_2 may result in the CT-CT coherence appearing in the spectrum as well as the ST_1 -CT coherence. Cycling of ϕ_1 results in as yet undetermined lines appearing in the spectrum. Although it has been stated that CT-CT transitions cannot be removed from the spectrum [45], clearly this study shows that phase cycling does have an influence over appearance of these transitions. A possible explanation might be that phase cycles of 1 and 2 produce a wider variety of coherence orders than the 4 phase cycle. According to Equation 2.139, a phase cycle of 1 allows $0, \pm 1, \pm 2, \dots$ coherence orders. A phase cycle of 2 allows $\dots -3, -1, 1, 3, \dots$ coherence orders. On the other hand, a 4 phase cycle would only allow $\dots -4, 1, 5, \dots$ coherence orders. Receiver phase cycling defined in Equation 3.3 may not be able to completely remove the allowed coherence orders for phase cycles of 1 and 2.

Chapter 4

The Lee-Goldburg Experiment

The Lee-Goldburg (LG) experiment was first performed in 1965 [26]. It involves the application of an rf field that includes an offset frequency added to the on-resonance frequency. This gives rise to a magnetic field in the rotating frame that lies at the magic angle to the z-axis. This technique has been applied in decoupling during observation as well as in two dimensional cross-polarization experiments that give the heteronuclear dipolar frequency splitting. In this chapter, I describe the mechanics of the LG experiment.

4.1 Decoupling

The dipolar interaction can contribute to rapid transverse relaxation. As already stated, this broadens signals in the frequency domain. In order to resolve peaks which are close to one another, it is desirable to attenuate the broadening. Sample spinning is a means of doing this mechanically. It can also be done with application of rf fields. Nuclei which are not being directly observed are usually decoupled if they will significantly broaden the signal of interest.

4.1.1 General Decoupling

Decoupling usually refers to heteronuclear interactions. Many times it is desirable to remove interactions that occur between a nucleus being observed and the other different nuclei surrounding it. Heteronuclear spin interactions can be cast in a form

$$\mathcal{H}_{spin} \sim \mathbf{I} \cdot \mathbf{T} \cdot \mathbf{S} \quad (4.1)$$

where I and S are spins and T is the interaction tensor. These types of interactions will change sign with a change in the state of the spin. The key to most decoupling techniques is to apply on-resonance rf pulses that flip the spin from one Zeeman state to another over the observation time. This effectively averages the heteronuclear spin interactions to zero. Two Pulse Phase Modulation (TPPM) is one means of doing this. TPPM decouples the dipolar and J-coupling interactions.

4.1.2 Lee-Goldburg Decoupling

LG techniques involve the irradiation of a sample with an off-resonance pulse. The effect of this technique is most easily seen in the rotating frame. Consider Equation 2.11, where the effective field is explicitly separated out,

$$i\hbar \frac{\partial \Psi'}{\partial t} = -[\hbar(\omega_{rf} + \gamma B_0)I_z + \gamma \hbar B_{rf} I_x] \Psi' \quad (4.2)$$

$$= -\gamma(\mathbf{B}_{eff} \cdot \mathbf{I}) \Psi' \quad (4.3)$$

B_{eff} will have both a z and an x component in general. The direction of the effective field relative to the z-axis is

$$\tan \theta_{B_{eff}} = \frac{\gamma B_{rf}}{(\omega_{rf} + \gamma B_0)} \quad (4.4)$$

For judiciously chosen B_{rf} and ω_{rf} , $\tan \theta_{B_{eff}}$ will take the value of the magic angle, $\sqrt{2}$. In practice, ω_{rf} is calculated for a set value of B_{rf} . A diagram of the effective field in the rotating frame is given in Figure 4.1.

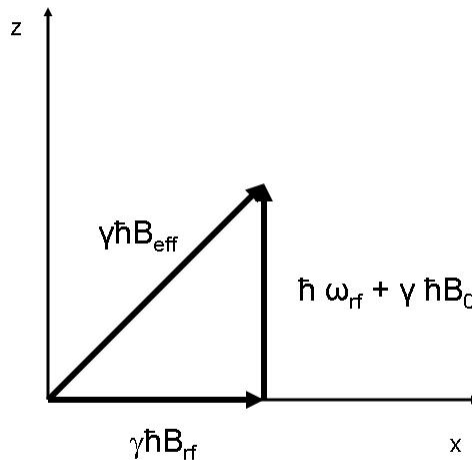


Figure 4.1: Representation of Lee-Goldburg vectors in the rotating frame.

This technique is used to decouple homonuclear interactions while leaving heteronuclear interactions intact but scaled. The nucleus to which the LG decoupling is applied is precessing about the magic angle in the rotating frame. Thus the first order terms in the homonuclear spin interactions which contain second order Legendre polynomials will be averaged to zero. The heteronuclear spin interactions will still affect the system and thus leave them able to be

observed. As mentioned, they will be scaled. The scale factor is determined from the component of the decoupled nucleus which lies along the Zeeman axis. For LG decoupling, this is

$$\cos \theta_m = \frac{1}{\sqrt{3}} \quad (4.5)$$

where θ_m is the magic angle.

4.2 J-Coupling Results in Guanosine

J-coupling in solids has not received much attention in the past due to its relatively small interaction energies compared with dipolar and chemical shielding interactions [11]. However, scalar couplings are very sensitive to local bonding structure and can be exploited to give detailed information on bonding environments [11, 41]. Claramunt et al. [40] have indirectly measured the ^{15}N - ^{15}N hydrogen bond scalar coupling in a pyridine-pyridinium tetrachlorogallate using a CP MAS spin-echo experiment and fitting of the peak intensity integrals to a model signal intensity. In 2005, Cornago et al., measured a ^{15}N - ^{19}F coupling in an organometallic complex [32]. Pham et al., has indirectly measured the N1-N7 hydrogen bond mediated scalar coupling in guanosine using a rotor synchronized Hahn echo pulse train [50]. There has been no report of hydrogen bond effects on solid state spectral peak positions seen with LG off-resonance experiments. In addition, no reports have shown a solid state ^{15}N -H scalar coupling in guanosine.

Guanosine is a nucleoside which can be phosphorylated to become guanosine monophosphate, guanosine diphosphate, and guanosine triphosphate. Each of these are involved in biochemical processes ranging from nucleic acid and protein synthesis to photosynthesis and muscle contraction [13]. The chemical

structure is depicted in Figure 4.2 with the N-H bonded atoms highlighted [52]. All figures of molecules in this work were created with Jmol [54]. The sample used in these experiments is a powdered crystal isotopically enriched with ^{15}N to 99% obtained from Cambridge Isotope Labs. The data was taken on a Varian 4.7 T magnet with the sample confined to a 4 mm sphere in the center of the coil to ensure rf homogeneity. The sample was subjected to a spinning speed of 10 kHz. Figure 4.2 shows the ^{15}N resonance spectrum with N1 resonance lines labeled. Two pulse phase modulation (TPPM) was used to remove dipolar coupling [3]. All the resonances can be assigned from prior work [12, 18]. The N2 lines in this spectrum are not resolved due to proton broadening of the N-H₂. Also, the most intense peak in the spectrum contains both an N9 and N3 peak which are unresolved.

There are two lines for every N in the spectrum due to there being two chemically inequivalent sites in the asymmetric unit of the guanosine crystal [50]. Figure 4.3 shows the orientation of two molecules with hydrogen bonding N1-N7.

The scalar coupling between the nitrogen and hydrogen in the N-H bonds was computed with Gaussian ab initio quantum chemical software [16]. Density functional theory (DFT) was used with the appropriate functional for accurate J-coupling as described in the work by Lantto, et al. [33]. The functional is the 3 parameter Becke-Lee-Yang-Parr (B3LYP) functional. In the Lantto paper, DFT results were compared to experimental data to validate its accuracy. Maximum percent errors were 6%.

Gaussian calculates the total spectral contribution of the J-coupling Hamiltonian. Inputs to the computation are the atomic positions of guanosine nuclei. X-ray data was used to determine the positions of nuclei heavier than hydrogen. Gaussian was used to energetically optimize the hydrogen positions.

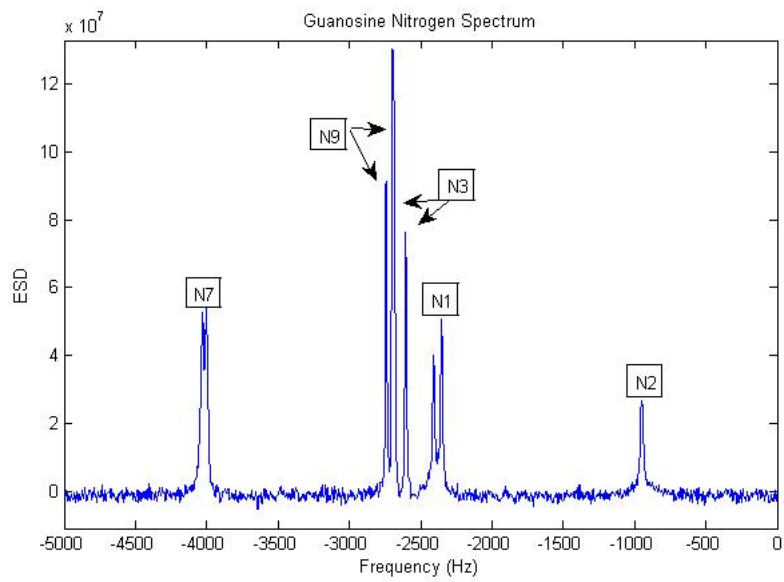
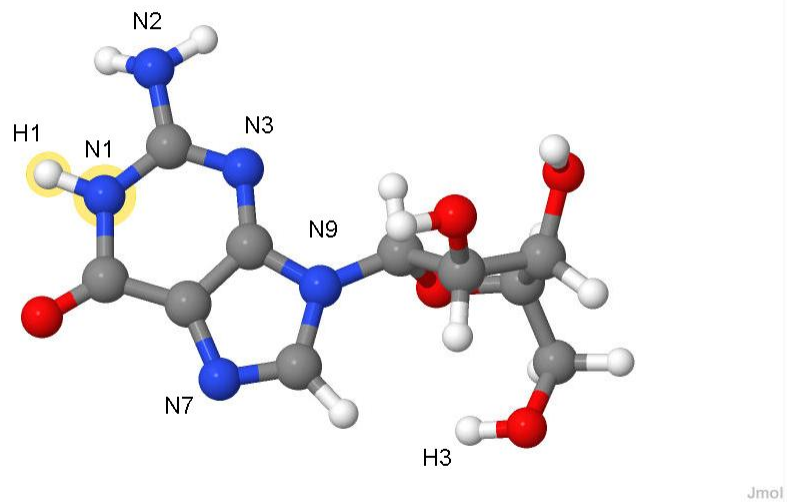


Figure 4.2: Guanosine molecule with the N1-H1 portion highlighted and the ^{15}N spectrum with resonance peaks labeled.

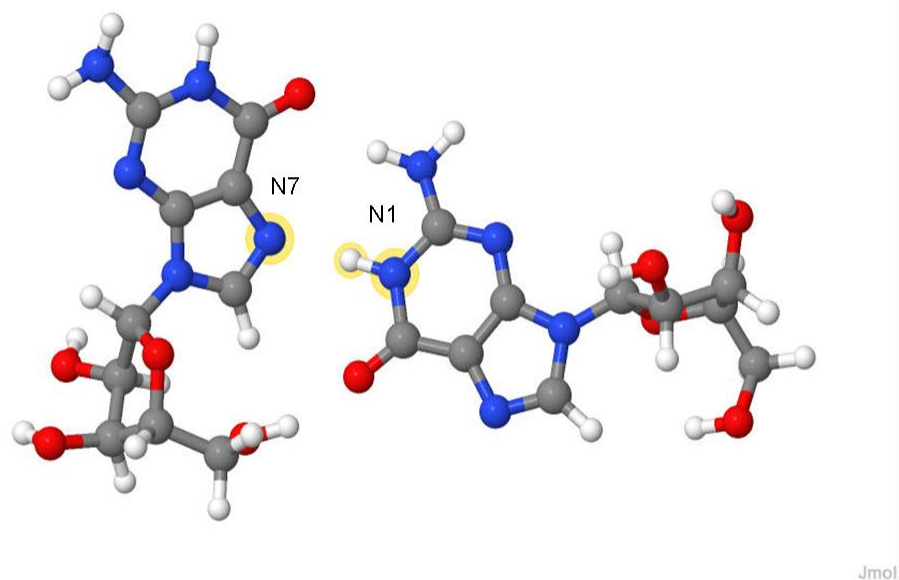


Figure 4.3: Molecules of guanosine showing orientation in the crystal for the N1-N7 hydrogen bond. Highlights show the nitrogen and hydrogen atoms involved in the hydrogen bond.

Gaussian adjusts the geometry of hydrogen nuclei on the potential surface until a minimum is found [16]. Standard deviations for x-ray data bond lengths are 0.004 \AA [52, 9]. This gives an error in the calculated frequencies of 0.00003 Hz for a bond length of $1.02 \pm 0.004 \text{ \AA}$. Table 4.1 gives the theoretical scalar couplings in both the hydrogen bonded (H-bond) and isolated molecule cases. In the H-bonded case, the calculation involved two guanosine molecules in their crystal orientation. Two molecules are sufficient since J-coupling involves the bond between atoms. The single molecule case involved an isolated guanosine molecule.

Figure 4.4 shows experimental data for the CP experiment with LG decoupling. To determine the offset frequency, an array of offset frequencies were tested and the one with the best resolution was chosen. It is apparent that the N1 spectral lines have broadened and split. Full width at half max of the

Table 4.1: Computed scalar couplings for guanosine. N1-H1 refers to the donor nitrogen. N7 refers to the acceptor nitrogen. The H-bond was calculated with two guanosine molecules while the absence of the H-bond was calculated with a single molecule.

Guanosine J-Coupling (Hz)		
	One Molecule	Two Molecules
N1-H1	93.79	92.99
N7	-	3.967

N1 portion of the spectrum is measured at 120 Hz. The maximum dipolar coupling for an N1-H1 bond length measurement of 1.04 Å is 10.8 kHz, calculated using Equation 2.74. Dipolar coupling is effectively removed by sample spinning at 10kHz. The evident splitting in the lines must come from the scalar coupling.

N1-H1 scalar couplings will split the N1 lines into doublets centered about the TPPM peaks [1]. Since there are 2 N1 lines due to inequivalent sites in the crystal, there should be 4 peaks in the spectrum. Figure 4.5 is an overlay of the N1 lines for the TPPM and LG decoupled spectra. Each line in the TPPM spectra has split into centered doublets. To determine the splitting, the curve was fit with a superposition of 4 Lorentzian functions. The form of the functions is

$$f(x; c_i, g_i, x_i) = \frac{c_i g_i}{(x - x_i)^2 + g_i^2} + c_0 \quad (4.6)$$

where c_i , g_i , x_i , and c_0 are parameters of the fit and $i = 1...4$. Figure 4.6 gives the experimental data versus the fit. The fitted parameters and the goodness of fit are given in table 4.2.

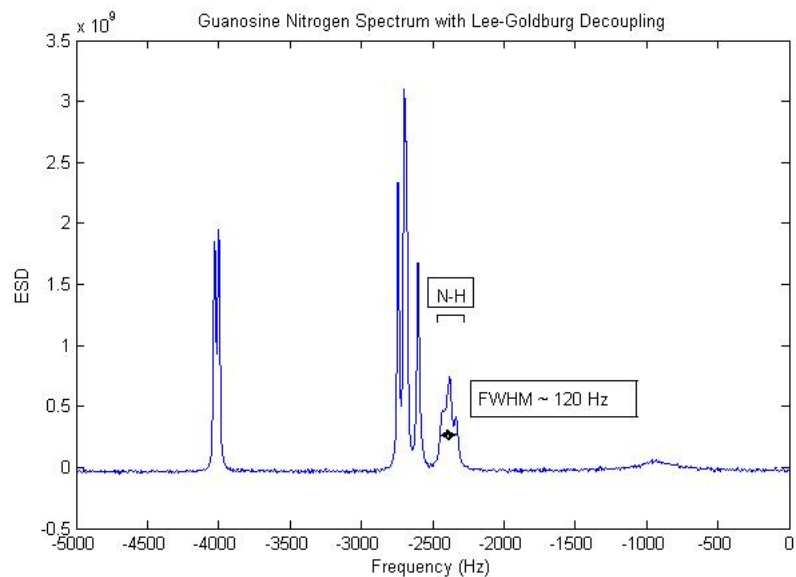


Figure 4.4: Guanosine ^{15}N cross polarization with LG decoupling.

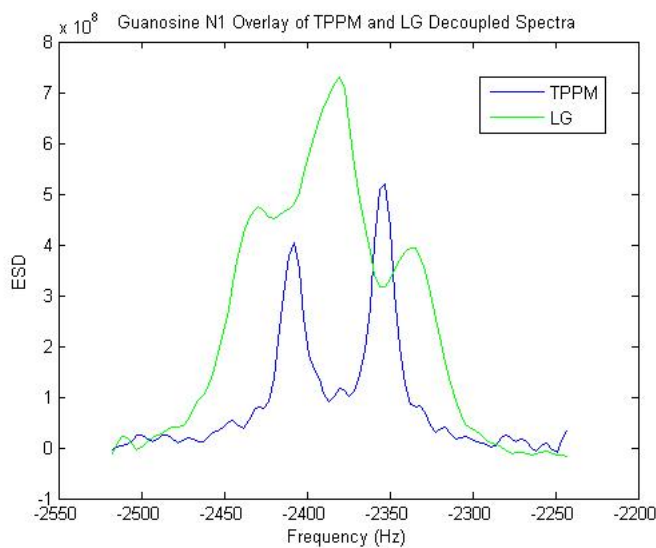


Figure 4.5: Guanosine N1 peaks for TPPM and LG decoupled data. The TPPM decoupled data was magnified 10 times to make comparison more clear.

The N1-H1 frequency splitting values provided by the fit are

$$F_1 = x_1 - x_2 = 36 \pm 12\text{Hz} \quad (4.7)$$

$$F_2 = x_3 - x_4 = 44 \pm 3\text{Hz} \quad (4.8)$$

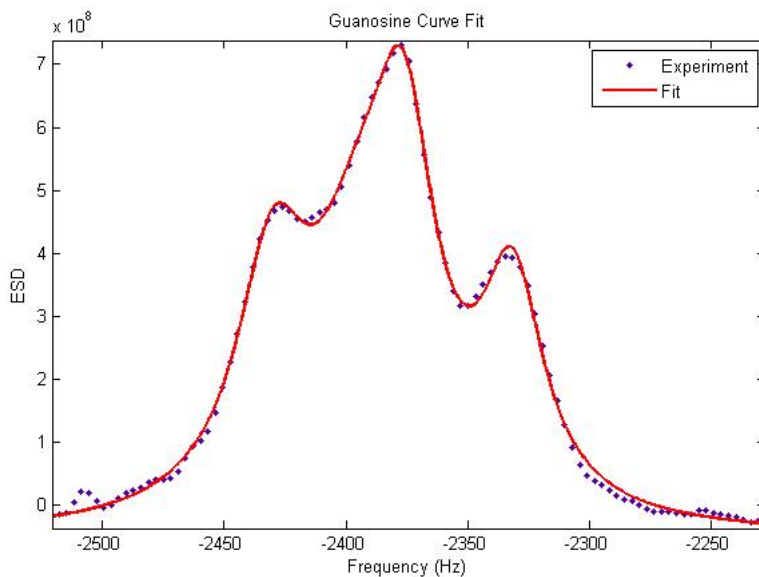


Figure 4.6: Fitting of the N-H splitting in the Lee-Goldburg decoupled spectrum of guanosine.

Table 4.2: Guanosine curve fitting parameters and goodness of fit data. Units for g_i and x_i are in Hz.

Guanosine N-H Curve Fit	
R-square	0.9983
Coefficients (with 95% confidence bounds)	
c_0	-5.221e+007 (-6.357e+007, -4.084e+007)
c_1	6.494e+009 (4.241e+009, 8.747e+009)
c_2	9.293e+009 (-2.505e+009, 2.109e+010)
c_3	6.821e+009 (-4.387e+008, 1.408e+010)
c_4	5.403e+009 (4.554e+009, 6.252e+009)
g_1	17.93 (15.1, 20.75)
g_2	25.38 (12.14, 38.62)
g_3	15.14 (9.997, 20.29)
g_4	15.46 (13.99, 16.93)
x_1	-2430 (-2431, -2429)
x_2	-2394 (-2405, -2383)
x_3	-2376 (-2378, -2374)
x_4	-2332 (-2332, -2331)

Using the experimental results and computed values of scalar coupling, the scale factors are given in Table 4.3. Scale factors are determined to be less than the theoretically predicted values. The choice of offset frequency is largely

responsible for this difference, since the offset was chosen to give the best empirical results. A scale factor of 0.577 gives an angle in the rotating frame corresponding to the magic angle, 54.7° . A scale factor of 0.47 gives an angle of 62.0° . The largest scale factor within the errors for the data is 0.516 which gives an angle of 58.9° . In the literature, scale factors rarely match 0.577 but are found to be closer to 0.50 [53, 7]. Reasons for this are unclear.

Table 4.3: Guanosine calculated scale factors.
Guanosine N-H Scale Factors

Experiment (Hz)	Calculated (Hz)	Scale Factor $\frac{Exp}{Calc}$
36 ± 12	93.79 No H-bond	0.38 ± 0.13
	92.99 H-bond	0.39 ± 0.13
44 ± 3	93.79 No H-bond	0.47 ± 0.03
	92.99 H-bond	0.47 ± 0.03

In addition to the N1-N7 hydrogen bonds, the N3 hydrogen bonds to an oxygen through the H3 of another molecule in the crystal. N9 does not hydrogen bond [52]. Table 4.4 gives the effect of hydrogen bonds on scalar coupling calculated with Gaussian. As indicated, the scalar couplings for hydrogen

Table 4.4: Computed scalar couplings for hydrogen bond acceptor N sites in guanosine. The H-bond was calculated with two guanosine molecules while the absence of the H-bond was calculated with a single molecule.

	Guanosine J-Coupling (Hz)	
	One Molecule	Two Molecules
N7	0	3.967
N3	0	3.534

bonds are on the order of Hertz and are small compared to line widths in the spectrum ≈ 30 Hz. Typically, effects of such small interactions are not observed in SSNMR. Figure 4.7 and Figure 4.8 show the fits of the other peaks in the spectrum of Guanosine both for TPPM and LG decoupling, respectively.

Table 4.5 gives the fitted peak positions for both spectra. The fitted peak

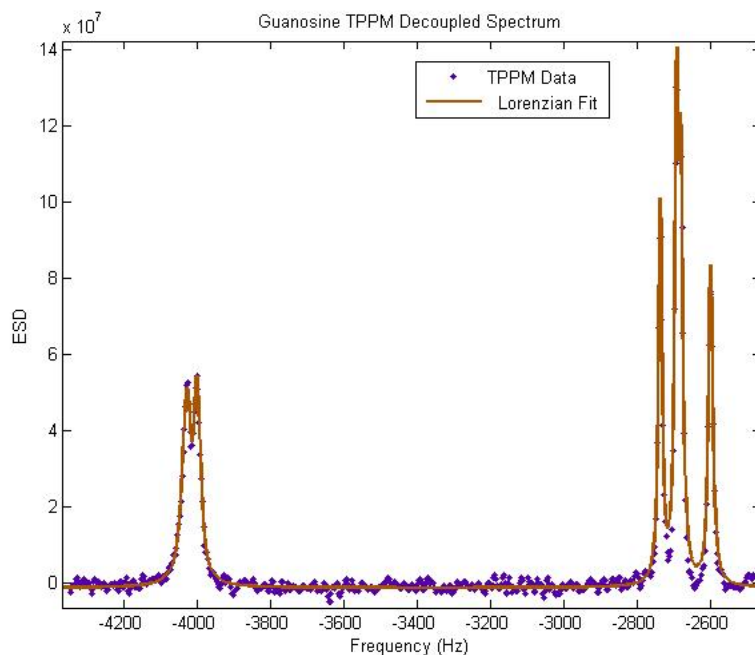


Figure 4.7: The fitted guanosine spectrum of TPPM decoupled data.

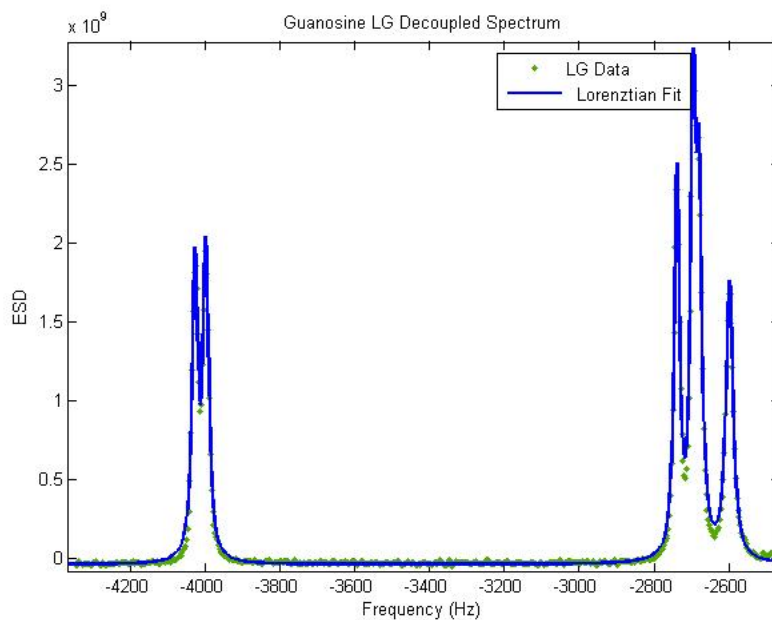


Figure 4.8: The fitted guanosine spectrum of LG decoupled data.

positions for the two experiments show a trend consistent with J-coupling effects from hydrogen bonding, i.e. the J-coupling interaction has a non-zero scalar coupling constant which shifts peaks in the spectrum. In particular,

Table 4.5: Guanosine curve fitting peak parameter values for TPPM and LG decoupled spectra. Units are in Hz and values in parentheses are the 95% confidence bounds.

Guanosine N-H Curve Fit		
R-square	0.9842	
	Peak Positions	
	TPPM Decoupling	LG Decoupling
N7a	-4028 (-4029, -4027)	-4026 (-4027, -4026)
N7b	-4000 (-4001, -3999)	-3998 (-3998, -3998)
N9a	-2739 (-2739, -2739)	-2739 (-2739, -2739)
N9b	-2694 (-2694, -2694)	-2695 (-2696, -2695)
N3a	-2683 (-2683, -2683)	-2681 (-2681, -2680)
N3b	-2601 (-2602, -2601)	-2598 (-2599, -2598)

the N7 and N3 nitrogens show fitted shifts of ≈ 2 or 3 Hz between experiments. The resolved N9 peak shows no fitted peak shift. There are a couple issues to consider. First, the resolution within a spectrum is about 12.2 Hz. This is determined by visually determining when the signal decays into the noise. The true resolution may be smaller than 12 Hz. Second, there are phasing considerations between the spectra, which may give rise to errors. Looking at variations in the phasing of spectra show that peak positions are not significantly influenced by spectral phasing up to several degrees allaying this concern. Thirdly, there is the inherent noise within each spectrum. The TPPM experiment has a lower signal to noise due to fewer acquisitions. The lowest signal to noise ratio is 50:1. This large signal to noise discounts variations in peak positions due to noise. Finally, the static magnetic field of the magnet may drift over time. This last concern would seem to be resolved since a field drift would cause a shift in all lines in the spectrum, but the resolved N9 line shows no shift.

In conclusion, results from these LG decoupling experiments in guanosine are important for 3 reasons. First, directly obtaining a J-coupling in solids is noteworthy. Since J-coupling constants are typically orders of magnitude

smaller than other interactions, they are not normally observable. Second, the calculated scale factors show a difference from the theoretical value. Such results are also seen in the literature. This indicates a need for further research to explain discrepancies in scale factor. Thirdly, the indication that hydrogen bonds may shift peaks in the spectra of solids due to scalar couplings is a new result. If this is correct, there may be small corrections to J-coupling necessary in the calculation of chemical shift tensors of hydrogen bonded nuclei which use isotropic peaks to determine tensor components.

4.3 Lee-Goldburg Cross Polarization

The LG technique was originally applied to decoupling during observation. However, in 1994 it was used in a 2 dimensional experiment to measure $^1\text{H}-^{15}\text{N}$ distances in a single crystal of acetylleucine [8]. This has led to a variety of applications of LG techniques used to determine heteronuclear couplings.

4.3.1 Cross Polarization

Cross polarization (CP) was first introduced in NMR as a means of increasing the signal of low abundance nuclei [48]. It is accomplished by transferring magnetization from high abundance to low abundance nuclei. Figure 4.9 gives the pulse sequence. Pulses specifically affect either I or S spins based on the respective resonant frequencies of the nucleus. The abundant I nuclei have magnetization placed along the x-axis in the rotating frame by a $\frac{\pi}{2}$ pulse. The I magnetization is locked along the x-axis in the rotating frame by an rf field of B_I . At the same time, a field of B_S is applied to the S spins. The applied

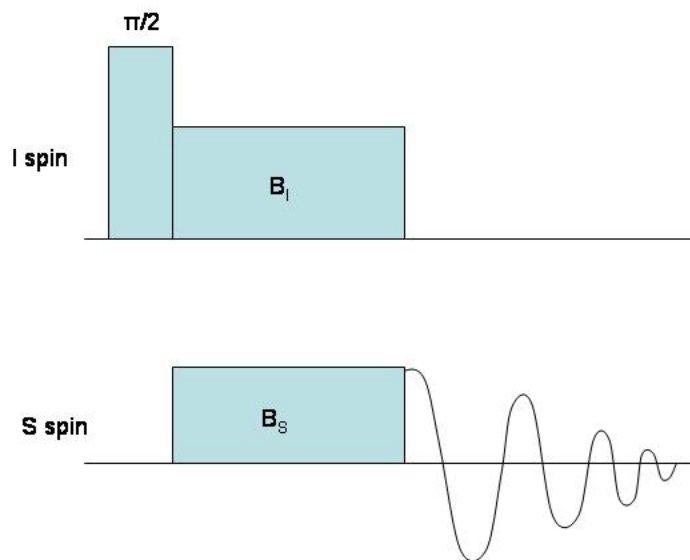


Figure 4.9: The cross polarization pulse sequence. A $\frac{\pi}{2}$ pulse is applied to the abundant I spins before the cross polarization pulses are applied.

fields are related as

$$\gamma_I B_I = \gamma_S B_S \quad (4.9)$$

When this condition is met, both spins have the same precession rate in their respective rotating frames. The time during which the spins are both irradiated, called the contact time, magnetization from the I spins is transferred to the S spins via the dipolar coupling. This gives an increase in the S signal. During observation, normal decoupling is usually applied to the I spins.

The pertinent Hamiltonian for this system in the rotating frames of both I and S taking into account only rf and dipolar terms is

$$\mathcal{H}_{CP} = -\gamma_I B_I I_x - \gamma_S B_S S_x + \mathcal{H}_{II} + \mathcal{H}_{SS} + \mathcal{H}_{IS} \quad (4.10)$$

The first two terms come from rf irradiation. The rest of the terms are homonuclear and heteronuclear dipolar contributions. If initially the I magnetization is along the x-axis, and at $t = 0$ the cross polarization rf pulses are turned on, then at this instant $\gamma_S B_S S_x = 0$. Interacting terms in the Hamiltonian are those that do not commute. We see that development of an S magnetization must come from $\gamma_I B_I I_x$ interacting with the IS dipolar term. This is the means by which energy is transferred between spins.

4.3.2 Lee-Goldburg Cross Polarization

Lee-Goldburg Cross Polarization (LGCP) is performed by subjecting spin I to off-resonance LG irradiation while spin S is irradiated on-resonance. As in LG decoupling, this removes homonuclear coupling between I spins and leaves the heteronuclear IS coupling. The pulse sequence is similar to that of normal cross polarization. However, the contact time is a variable. This gives 2 dimensional data in the time domain. The dimension corresponding to the variable CP time is termed the evolution dimension. The other dimension is the observation, or signal detection dimension.

Since the I spins are precessing about the magic angle in the rotating frame of I , there will be a decrease in the magnetization transfer between spins. The signal in a LGCP experiment will be less intense than in a normal CP experiment for the same contact time.

4.4 Results Dipolar Coupling in Guanosine

LGCP experiments have been used to determine C-H inter-nuclear distances in SSNMR, though there have been no reports of LGCP experimental results on nitrogens in guanosine. Removal of homonuclear dipole coupling for abundant

nuclei in a sample while leaving heteronuclear dipole coupling intact allows the measurement of heteronuclear distances. The dipole coupling constant given by Equation 2.74 is used to determine the distances.

Data on guanosine was collected on a Varian Infinity Plus 14.09 T magnet using a 3.2 mm rotor. Spinning speed was set to 10 kHz. The on-resonance frequency for ^1H was set at 599.792853 MHz. The frequency offset is 47.457 kHz, determined using Equation 4.4. The 2-dimensional LGCP data for guanosine is given in Figure 4.10. The F_1 axis represents the dipolar coupled dimension while the F_2 axis represents the isotropic dimension. Taking cross sections of

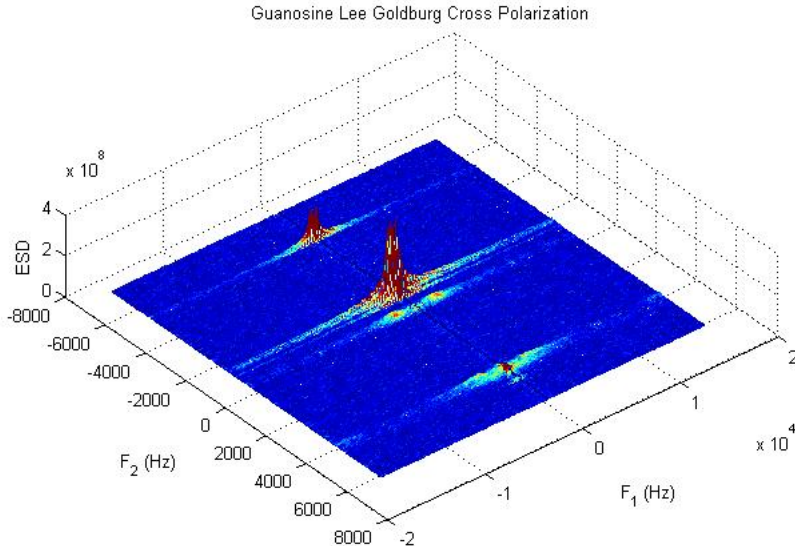


Figure 4.10: The Lee-Goldburg cross-polarization spectra of ^{15}N in 100% enriched guanosine.

the 2-dimensional data, we get the dipolar coupled information for the nitrogen peaks. Figure 4.11 shows the cross section for an N1 peak. Peaks labeled “SS” are due to sample spinning. Due to the build up of signal in the dipolar coupled dimension, there is a large average signal at 0 frequency. This signal has been suppressed in all the cross sections presented, since it contains no useful distance information. Also, as the frequency gets close to 0 Hz, there

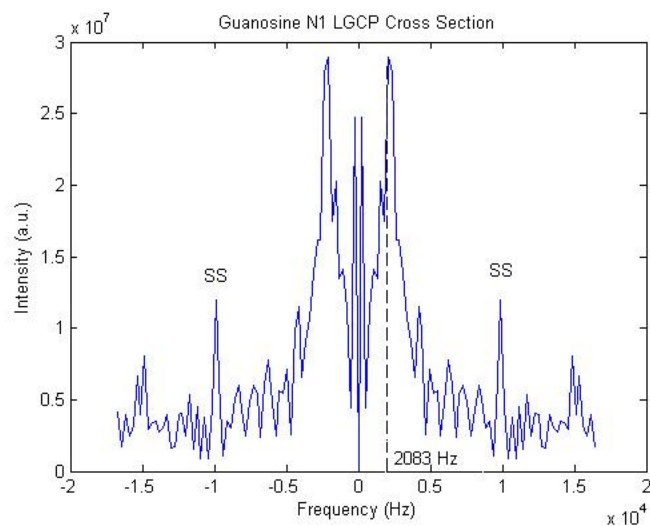


Figure 4.11: The Lee-Goldburg cross-polarization cross section for an N1 peak in guanosine.

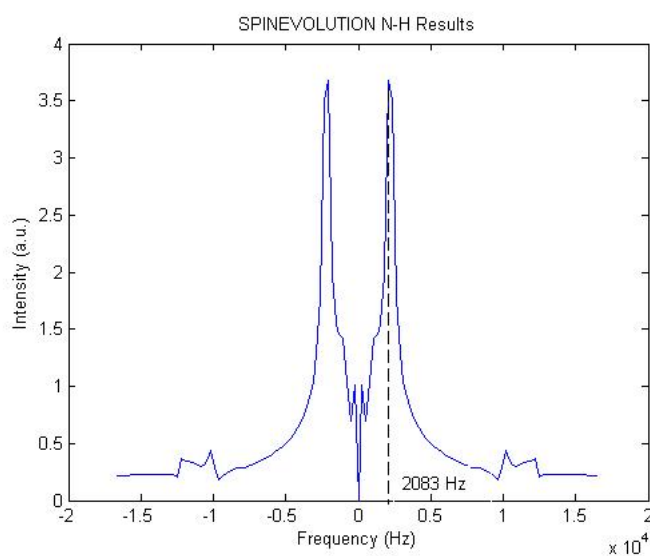


Figure 4.12: SPINEVOLUTION simulation for an N-H dipolar coupled bond with bond length of 1.04 \AA .

is a build up of signal from dipolar coupled nuclei within increasingly larger distances from each observed nucleus.

To corroborate experimental data, simulations of the experiment were performed using SPINEVOLUTION [29]. Only appropriate bond configurations were simulated, i.e. N-H and N-H₂. Figure 4.12 shows simulation results for

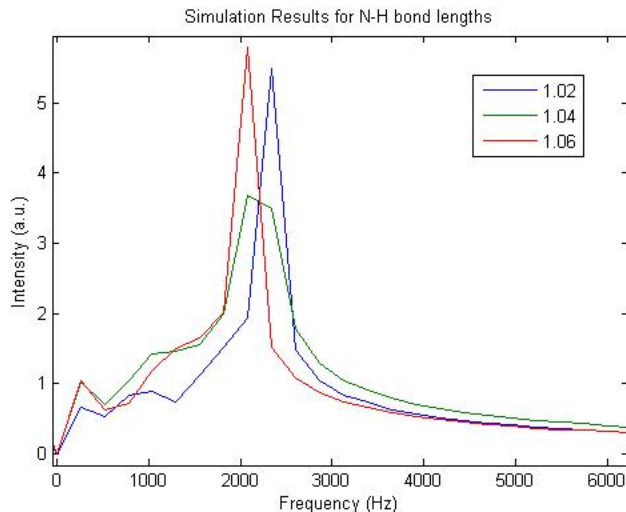


Figure 4.13: SPINEVOLUTION simulation for an N-H dipolar coupled bond with bond lengths from 1.02 to 1.06 Å.

an N-H dipolar coupled bond with a bond length of 1.04 Å. Figure 4.13 shows simulated results for bond lengths of 1.02, 1.04, and 1.06 Å. Peaks for smaller changes in bond lengths are not easily distinguished. So the uncertainty in bond length in the simulation is of the order of 0.02 Å.

Scale factors were determined from comparison to theory. For N1, a bond length of 1.04 Å gives a theoretical frequency of 10.823 kHz. The calculated scale factor is $\frac{\text{theory}}{\text{experiment}} = \frac{10.823\text{kHz}}{4.166\text{kHz}} = 2.6 \pm 0.08$. The uncertainty in experimental frequency is ± 130 Hz. As described in Section 4.2, the N1-H1 distance calculated from X-ray data by optimization of H positions is 1.03 Å.

Figure 4.14 is the experimental cross section for an N2 peak. Figure 4.15 shows the simulation results for bond lengths of 1.07 and 1.07 Å. Due to strong H-H dipolar coupling, changes in results for varying the bond length of one N-H bond show small changes in the simulated spectra. Figure 4.16 shows simulation results for one of the N-H bonds held at 1.07 Å and the other N-H bond varied by 1.05, 1.07, and 1.09 Å. Calculation from X-ray data for the two H atoms give 1.01 and 1.02 Å. Simulation results with these bond lengths

is given in Figure 4.17. Based on these data, it appears that the experimental results match simulation results better than the x-ray optimized data.

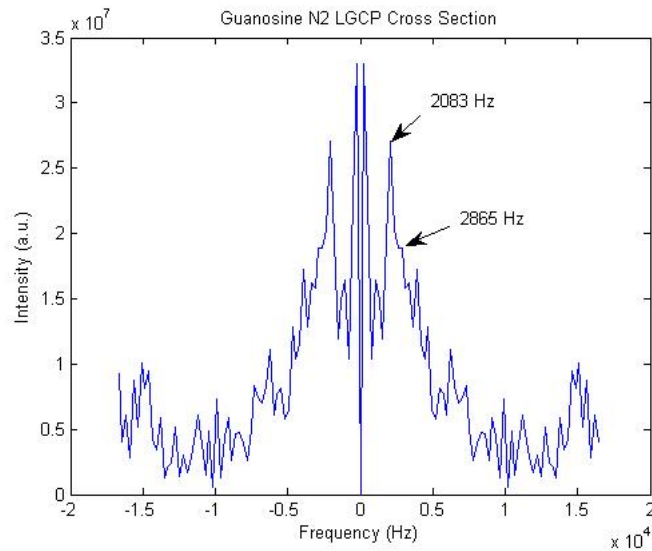


Figure 4.14: The Lee-Goldburg cross-polarization cross section for an N2 peak in guanosine.

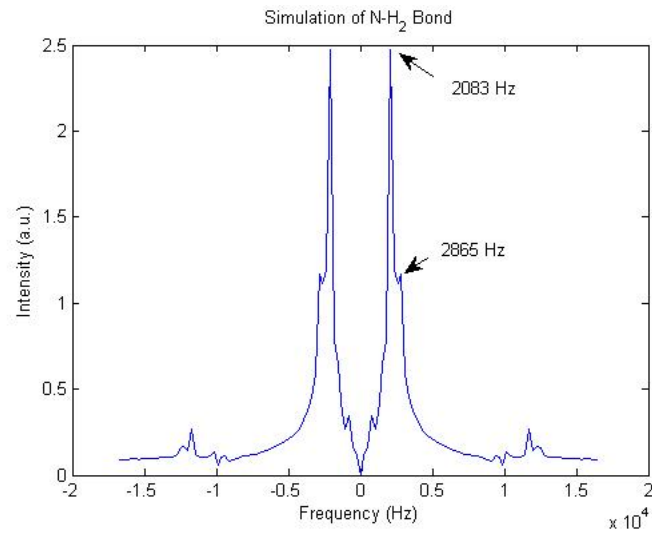


Figure 4.15: SPINEVOLUTION simulation for an N-H₂ dipolar coupled bond with bond lengths of 1.07 and 1.07 Å.

For the N7 nitrogens which are hydrogen bond acceptors, a distance of 1.84 Å to the nearest H1 is calculated from X-ray data. Figure 4.18 shows the LGCP cross section. The arrow indicates the possible signal from N7-H1

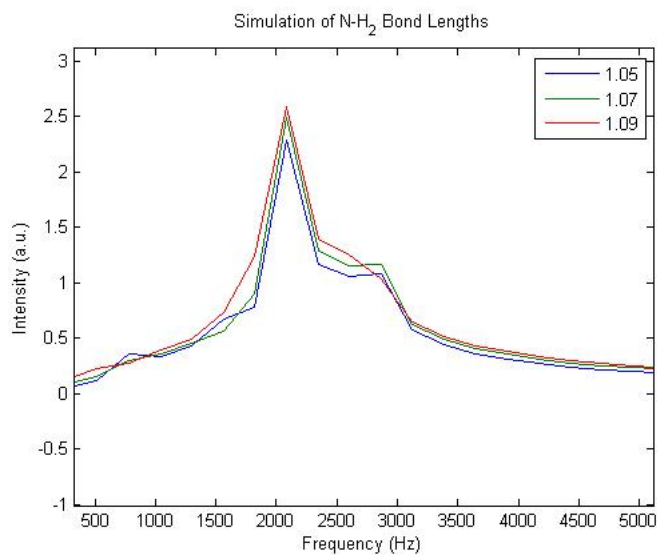


Figure 4.16: SPINEVOLUTION simulation for an N-H₂ dipolar coupled bonds. One bond was held fixed at \AA while the other was varied with bond lengths from 1.05 to 1.09 \AA .

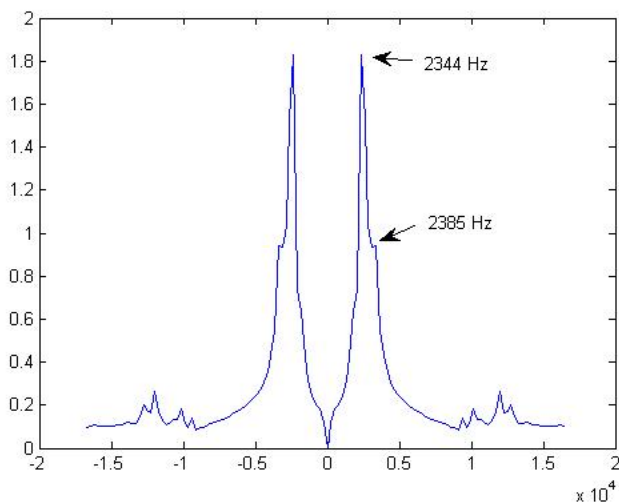


Figure 4.17: SPINEVOLUTION simulation for an N-H₂ dipolar coupled bonds with bond lengths of 1.01 and 1.02 \AA .

dipolar coupling. As frequencies go as inverse r^3 for dipolar couplings, nuclei further from the observed nucleus are more difficult to resolve. Figure 4.19 gives the simulation results for bond lengths of 1.6, 1.8, and 2.0 \AA . This shows that the error in bond length estimation grows as bond become longer.

In conclusion, it is shown that NMR-based N-H distance measurements

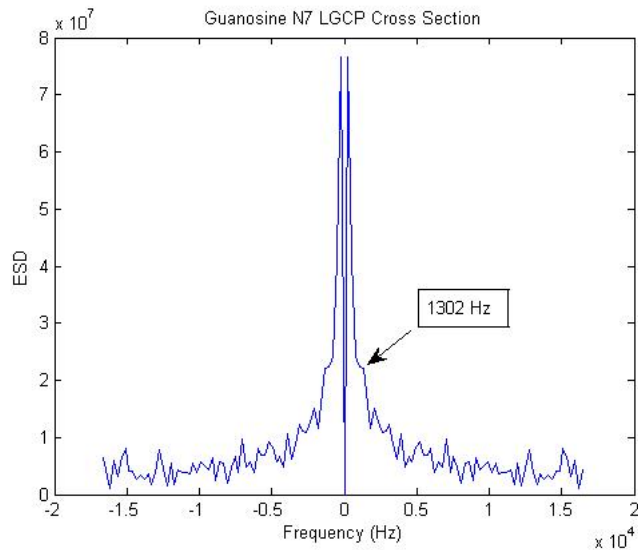


Figure 4.18: The Lee-Goldburg cross polarization cross section for N7.

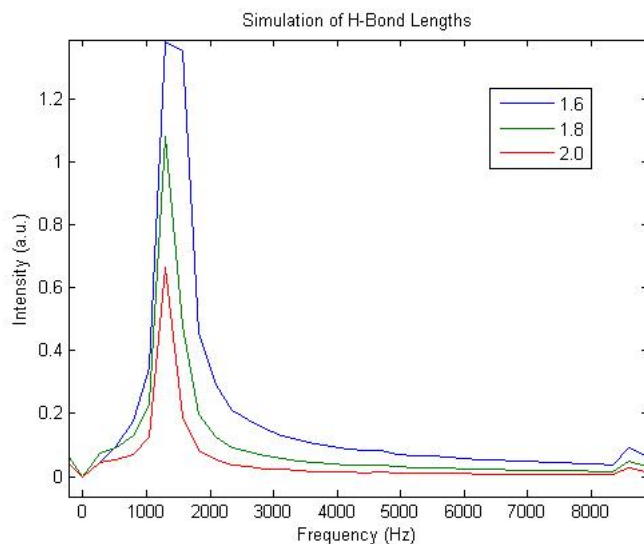


Figure 4.19: SPINEVOLUTION simulation for hydrogen bond lengths. Length units are in Å.

on guanosine show good agreement with simulation results. X-ray optimized data show good agreement for N-H distances but results appear to be in less agreement for N-H₂ bonds. Also, it is shown that hydrogen bond distances are accessible to SSNMR, though more resolution in the dipolar coupled dimension is required to make accurate measurements of these longer bonds.

Chapter 5

Conclusions

Off-resonance excitation in SSNMR has been utilized in both decoupling and indirect observation for several decades. Its usefulness comes from the fact that it leaves heteronuclear dipole coupling as well as J-coupling intact in the observed spectrum. This provides a means of determining interatomic nuclear positions in molecules. Successful NMR crystallography depends on measuring internuclear distances of all types of nuclei. A relatively small number of results exist for J-coupling in SSNMR using off-resonance techniques. Results for dipolar coupling have enjoyed more popularity, with much of the work focusing on ^{13}C bonds with ^1H . A handful of results show effects of hydrogen bonds in SSNMR spectra. In this work, Lee-Goldburg off-resonance decoupling and cross polarization were successfully used for determination of ^{15}N distances to H in the biomolecule guanosine and the ^{15}N -H scalar coupling.

LG decoupling on guanosine reveals a ^{15}N - ^1H scalar coupling directly in the spectrum. The scale factor was calculated to be less than that which theory would predict. This results from the empirical setting of the offset frequency. The reason for the appearance of the scalar coupling for the empirically determined offset frequency is unclear. In addition to the observation of J-coupling,

a possible observation of shifts in the spectrum for hydrogen bond acceptor nuclei is presented.

LG cross polarization experiments performed on guanosine give N-H distance measurements. Data shows N-H distances which compare very closely to optimized x-ray structure distances for N-H bonds. Experimental results give an N-H bond distance of $1.04 \pm 0.02 \text{ \AA}$. Experimental results for N-H₂ bonds appear to match simulation data better than x-ray optimized data. Experimental results give an N-H₂ bond length of $1.07 \pm 0.02 \text{ \AA}$. Also, results provide a distance between a hydrogen bond acceptor N and the bonded H of $1.67 \pm 0.2 \text{ \AA}$. This would be the first direct NMR dipolar distance measurement of N-H hydrogen bonds using LGCP.

This work also addresses phase cycling considerations of satellite transition magic angle spinning experiments. Results generally show that the number of phases in the phase cycle of the 1QSTMAS experiments studied here may significantly alter the experiment.

Further directions for this work include investigations of the discrepancy in empirical and theoretical scale factors for off-resonance experiments showing J-couplings in the solid state. Also, interactions between guanosine and silica in organic semiconductors show potential for further investigation with NMR. The application of off-resonance to quadrupolar nuclei is an area that has not received great attention but may prove useful for illuminating field gradient orientations, providing information on local electronic bond structures.

Bibliography

- [1] Abragam A. *The Principles of Nuclear Magnetism*. Oxford: Clarendon Press, 1961.
- [2] Fersht A. *Structure and Mechanism in Protein Science*. W. H. Freeman and Company, 1999.
- [3] Bennett AE, Rienstra CM, Auger M, Lakshmi KV, and Griffin RG. Heteronuclear decoupling in rotating solids. *J Chem Phys*, 103:6951, 1995.
- [4] Elena B, Pintacuda G, Mifsud N, and Emsley L. Molecular structure determination in powders by nmr crystallography from proton spin diffusion. *J Am Chem Soc*, 128:9555, 2006.
- [5] Gerstein BC. Combined rotation and multiple pulse spectroscopy. *Encyclopedia of NMR*, 1996.
- [6] Sanctuary BC. Multipole operators for an arbitrary number of spins n. *JCP*, 64:4352, 1975.
- [7] Coelho C, Rocha J, Madhu PK, and Mafra L. Practical aspects of lee-goldburg based cramps techniques for high-resolution 1-h nmr spectroscopy in solids: implementation and applications. *J Mag Res*, 194:264, 2008.
- [8] Wu CH, Ramamoorthy A, and Opella SJ. High resolution heteronuclear dipolar solid state nmr spectroscopy. *J Mag Res A*, 109:270, 1994.
- [9] Cramer CJ. *Essential of Computational Chemistry*. Wiley, 2002.
- [10] Slichter CP. *Principles of Magnetic Resonance*. Springer-Verlag, 1990.
- [11] Massiot D, Fayon F, Deschamps M, Cadars S, Florian P, Montouillout V, Pellerin N, Hiet J, Rakhmatullin A, and Bessada C. Detection and use of small j couplings in solid state nmr experiments. *C. R. Chimie*, 13:117, 2010.
- [12] Stueber D and Grant DM. 13-c and 15-n chemical shift tensors in adenosine, guanosine dihydrate, 2'-deoxythymidine, and cytidine. *J Am Chem Soc*, 124:10539, 2002.

- [13] Marks DB. *Biochemistry*. Baltimore: Williams and Wilkins, 1999.
- [14] Andrew ER. Magic angle spinning in solid state nmr spectroscopy. *Phil Trans R Soc A*, 299:505, 1981.
- [15] Abers ES. *Quantum Mechanics*. Pearson/Prentice Hall, 2004.
- [16] M. J. Frisch, G. W. Trucks, H. B. Schlegel, G. E. Scuseria, M. A. Robb, J. R. Cheeseman, G. Scalmani, V. Barone, B. Mennucci, G. A. Petersson, H. Nakatsuji, M. Caricato, X. Li, H. P. Hratchian, A. F. Izmaylov, J. Bloino, G. Zheng, J. L. Sonnenberg, M. Hada, M. Ehara, K. Toyota, R. Fukuda, J. Hasegawa, M. Ishida, T. Nakajima, Y. Honda, O. Kitao, H. Nakai, T. Vreven, J. A. Montgomery, Jr., J. E. Peralta, F. Ogliaro, M. Bearpark, J. J. Heyd, E. Brothers, K. N. Kudin, V. N. Staroverov, R. Kobayashi, J. Normand, K. Raghavachari, A. Rendell, J. C. Burant, S. S. Iyengar, J. Tomasi, M. Cossi, N. Rega, J. M. Millam, M. Klene, J. E. Knox, J. B. Cross, V. Bakken, C. Adamo, J. Jaramillo, R. Gomperts, R. E. Stratmann, O. Yazyev, A. J. Austin, R. Cammi, C. Pomelli, J. W. Ochterski, R. L. Martin, K. Morokuma, V. G. Zakrzewski, G. A. Voth, P. Salvador, J. J. Dannenberg, S. Dapprich, A. D. Daniels, Ö. Farkas, J. B. Foresman, J. V. Ortiz, J. Cioslowski, and D. J. Fox. Gaussian 09 Revision A.1. Gaussian Inc. Wallingford CT 2009.
- [17] Liddar H, Li J, Neogi A, Neogi PB, Sarkar A, Cho S, and Morkoc H. Self-assembled deoxyguanosine based molecular electronic device on gan substrates. *App Phys Lett*, 92:013309, 2008.
- [18] James Harper. Unpublished hetcor data.
- [19] Spiess HW. *Dynamic NMR Spectroscopy: Rotation of Molecules and Nuclear Spin Relaxation*. Springer-Verlag, 1978.
- [20] Trebosc J, Amoureux JP, and Gan ZH. Comparison of high-resolution solid-state nmr mpmas and stmas methods for half-integer quadrupolar nuclei. *Solid State Nuclear Magnetic Resonance*, 31:1, 2007.
- [21] Vaara J, Jokisaari J, and Wasylishen RE. Spin-spin coupling tensors as determined by experiment and computational chemistry. *Prog NMR Spec*, 41:233, 2002.
- [22] Waugh JS. Uncoupling of local field spectra in nuclear magnetic resonance: determination of atomic positions in solids. *Proc Natl Acad Sci*, 73:1394, 1976.
- [23] Harris KJ, Bryce DL, and Wasylishen RE. Line shapes from ab spin systems in solids - the role of antisymmetric spin-spin couplings. *Can J Chem*, 87:1338, 2009.

- [24] Frydman L and Harwood JS. Isotropic spectra of half-integer quadrupolar spins from bidimensional magic angle spinning nmr. *J Am Chem Soc*, 117:5367, 1995.
- [25] Duer M. *Introduction to Solid State NMR Spectroscopy*. Oxford, 2004.
- [26] Lee M and Goldburg W. Nuclear magnetic resonance line narrowing by a rotating rf field. *Phys Rev*, 140:A1261, 1965.
- [27] Munowitz M. *Coherence in Nuclear Magnetic Resonance*. Harvard Press, 1997.
- [28] Tinkham M. *Group Theory and Quantum Mechanics*. McGraw-Hill, 1964.
- [29] Veshtort M and Griffith RG. Spinevolution: A powerful tool for simulating solid and liquid state nmr. *J Mag Res*, 178:248, 2006.
- [30] Ramsey NF. The internal diamagnetic field correction in measurements of the proton magnetic moment. *Phys Rev*, 77:567, 1950.
- [31] Sorenson OW, Eich GW, Levitt MH, Bodenhausen G, and Ernst RR. Product operator formalism for the description of nmr pulse experiments. *Progress in NMR Spectroscopy*, 16:163, 1983.
- [32] Cornago P, Claramunt RM, Cano M, Heras JV, and Gallego ML. Multi-nuclear nmr study of pyroazole complexes to investigate the coordination mode. *Arkivoc*, ix:21, 2005.
- [33] Lantto P, Vaara J, and Helgaker T. Spin-spin coupling tensors by density-functional linear response theory. *J Chem Phys*, 117:5998, 2002.
- [34] Ernst R, Bodenhausen G, and Wokaun A. *Principles of Nuclear Magnetic Resonance in One and Two Dimensions*. Oxford University Press, 1994.
- [35] Hajjar R, Millot Y, and Man PP. Phase cycling in mqmas sequences for half-integer quadrupolar spins. *Prog NMR Spec*, 57:306, 2010.
- [36] Kubo R. *Statistical Mechanics*. Elsevier Science, 1999.
- [37] Liboff R. *Introductory Quantum Mechanics*. Addison-Wesley, 1998.
- [38] Paquin R, Pelupessy P, Duma L, Gervais C, and Bodenhausen G. Determination of the antisymmetric part of the chemical shift anisotropy tensor via spin relaxation in nuclear magnetic resonance. *J Chem Phys*, 133:034506, 2010.
- [39] Rinaldi R, Maruccio G, Biasco A, Arima V, Cingolani R, Giorgi T, Masiero S, Spada GP, and Gottarelli G. Hybrid molecular electronic devices based on modified deoxyguanosines. *Nanotechnology*, 13:398, 2002.

- [40] Claramunt RM, Perez-Torralba M, Maria DS, Sanz D, Elena B, Alkorta I, and Elguero J. 15-n 15-n spin-spin coupling constants through intermolecular hydrogen bonds in the solid state. *J Mag Res*, 206:274, 2010.
- [41] Cadars S, Lesage A, Trierweiler M, Heux L, and Emsley L. Nmr measurements of scalar-coupling distributions in disordered solids. *Physical Chemistry Chemical Physics*, 9:92, 2007.
- [42] Lena S, Masiero S, Pieraccini S, and Spada GP. Guanosine hydrogen-bonded scaffolds: A new way to control the bottom-up realisation of well-defined nanoarchitectures. *Chemistry-A European Journal*, 15:7792, 2009.
- [43] Paasch S and Brunner E. Trends in solid-state nmr spectroscopy and their relevance for bioanalytics. *Anal Bioanal Chem*, 398:2351, 2010.
- [44] Ashbrook SE. Recent advances in solid state nmr of quadrupolar nuclei. *Phys Chem Chem Phys*, 11:6892, 2009.
- [45] Ashbrook SE and Wimperis S. High resolution nmr in quadrupolar nuclei of solids: the satellite transition magic angle spinning (stmas) experiment. *Prog NMR Spec*, 45:53, 2004.
- [46] Ashbrook SE and Wimperis S. Satellite transition mas nmr of spin $i = 3/2, 5/2, 7/2, 9/2$ nuclei. *J Mag Res*, 156:269, 2004.
- [47] Hwang SJ and Gerstien BC. Spin counting in dipolar coupled spin $1/2$ systems by multiple quantum coherence. *Bull Mag Res*, 15:211, 1996.
- [48] Hartman SR and Hahn EL. Nuclear double resonance in the rotating frame. *Phys Rev*, 128:2042, 1962.
- [49] Farrar TC and Harriman JE. *Density Matrix Theory and Its Applications in NMR Spectroscopy*. Farragut Press, 1992.
- [50] Pham TN, Griffin JM, Masiero S, Lena S, Gottarelli G, Hodgkinson P, Phillip C, and Brown SP. Quantifying hydrogen-bonding strength: the measurement of $(2h)j(nn)$ couplings in self-assembled guanosines by solid-state n-15 spin-echo mas nmr. *Phys Chem Chem Phys*, 9:3416, 2007.
- [51] Haeberlen U. *High Resolution NMR in Solids: Selective Averaging*. Academic Press, 1976.
- [52] Thewalt U, Bugg C, and Marsh R. The crystal structure of guanosine dihydrate and inosine dihydrate. *Acta Cryst*, B29:1089, 1970.
- [53] van Rossum BJ, de Groot CP, Ladizhansky V, Vega S, and de Groot HJM. A method for measuring heteronuclear distances in high speed mas nmr. *J Am Chem Soc*, 122:3465, 2000.

- [54] www.jmol.org. Jmol: an open-source java viewer for chemical structures in 3d. <http://www.jmol.org/>.
- [55] Gan Z. Isotropic nmr spectra of half-integer quadrupolar nuclei using satellite transitions and magic angle spinning. *J Am Chem Soc*, 122:3242, 2000.
- [56] Gan Z. Satellite transition magic angle spinning nuclear magnetic resonance of half integer quadrupolar nuclei. *J Chem Phys*, 114:10845, 2001.